NAVAL POSTGRADUATE SCHOOL

MONTEREY, CALIFORNIA

THESIS

BIO-INSPIRED MEMS DIRECTION FINDING UNDERWATER ACOUSTIC SENSOR

by

Joshua D. Collins

September 2017

Thesis Advisor: Gamani Karunasiri
Co-Advisor: Fabio Alves

Approved for public release. Distribution is unlimited.

THIS PAGE INTENTIONALLY LEFT BLANK

REPORT DOCUMENTATION PAGE	*Form Approved OMB No. 0704-0188*

1. AGENCY USE ONLY ***(Leave blank)***	**2. REPORT DATE** September 2017	**3. REPORT TYPE AND DATES COVERED** Master's thesis

4. TITLE AND SUBTITLE BIO-INSPIRED MEMS DIRECTION FINDING UNDERWATER ACOUSTIC SENSOR	**5. FUNDING NUMBERS**
6. AUTHOR(S) Joshua D. Collins	
7. PERFORMING ORGANIZATION NAME(S) AND ADDRESS(ES) Naval Postgraduate School, Monterey, CA 93943-5000	**8. PERFORMING ORGANIZATION REPORT NUMBER**
9. SPONSORING /MONITORING AGENCY NAME(S) AND ADDRESS(ES) N/A	**10. SPONSORING / MONITORING AGENCY REPORT NUMBER**

11. SUPPLEMENTARY NOTES The views expressed in this thesis are those of the author and do not reflect the official policy or position of the Department of Defense or the U.S. Government. IRB number ____N/A____.

12a. DISTRIBUTION / AVAILABILITY STATEMENT	**12b. DISTRIBUTION CODE**
Approved for public release. Distribution is unlimited.	A

13. ABSTRACT (maximum 200 words)

This thesis has developed a microelectromechanical directional acoustic sensor based on directional finding capabilities that the *Ormia Ochracea* fly uses. Previous versions of this sensor have been characterized in the air to exploit resonance modes and resolve bearing ambiguity of an incident sound wave. New sensors have been designed and fabricated for use in the underwater environment. This thesis focuses on the development of these underwater sensors. The research involved design, simulation and experimental characterization of these sensors in both air and water. The sensors show readiness for further development and that they can be vital as a directional finding sound sensor in numerous undersea applications.

14. SUBJECT TERMS	**15. NUMBER OF PAGES**
MEMS, direction finding, *Ormia Ochracea*, acoustic sensor, underwater	115
	16. PRICE CODE

17. SECURITY CLASSIFICATION OF REPORT	**18. SECURITY CLASSIFICATION OF THIS PAGE**	**19. SECURITY CLASSIFICATION OF ABSTRACT**	**20. LIMITATION OF ABSTRACT**
Unclassified	Unclassified	Unclassified	UU

NSN 7540-01-280-5500 Standard Form 298 (Rev. 2-89)
Prescribed by ANSI Std. 239-18

THIS PAGE INTENTIONALLY LEFT BLANK

Approved for public release. Distribution is unlimited.

BIO-INSPIRED MEMS DIRECTION FINDING UNDERWATER ACOUSTIC SENSOR

Joshua D. Collins
Lieutenant, United States Navy
B.S., United States Naval Academy, 2010

Submitted in partial fulfillment of the
requirements for the degree of

MASTER OF SCIENCE IN ENGINEERING ACOUSTICS

from the

NAVAL POSTGRADUATE SCHOOL
September 2017

Approved by: Gamani Karunasiri
Thesis Advisor

Fabio Alves
Co-Advisor

Daphne Kapolka
Chair, Engineering Acoustics Academic Committee

THIS PAGE INTENTIONALLY LEFT BLANK

ABSTRACT

This thesis has developed a microelectromechanical directional acoustic sensor based on directional finding capabilities that the *Ormia Ochracea* fly uses. Previous versions of this sensor have been characterized in the air to exploit resonance modes and resolve bearing ambiguity of an incident sound wave. New sensors have been designed and fabricated for use in the underwater environment. This thesis focuses on the development of these underwater sensors. The research involved design, simulation and experimental characterization of these sensors in both air and water. The sensors show readiness for further development and that they can be vital as a directional finding sound sensor in numerous undersea applications.

THIS PAGE INTENTIONALLY LEFT BLANK

TABLE OF CONTENTS

THIS PAGE INTENTIONALLY LEFT BLANK

LIST OF FIGURES

THIS PAGE INTENTIONALLY LEFT BLANK

LIST OF TABLES

THIS PAGE INTENTIONALLY LEFT BLANK

LIST OF ACRONYMS AND ABBREVIATIONS

DF	Direction Finding
Gen	Generation
MEMS	Microelectromechanical Systems
Mod	Modification
NPS	Naval Postgraduate School
NUWC	Naval Undersea Warfare Center
PCB	Printed Circuit Board
Q	Quality Factor
SEM	Scanning Electron Microscope
SOIMUMPS	Silicon-on-Insulator Multi-user Manufacturing Process

THIS PAGE INTENTIONALLY LEFT BLANK

ACKNOWLEDGMENTS

The process of turning a fly’s ear into an effective sensor, one with numerous applications, is an ambitious and intriguing project, and I would like to thank all students who came before me, specifically my immediate predecessor, Will Swan.

Additionally, I want to emphatically thank my two thesis advisors, Dr. Gamani Karunasiri and Dr. Fabio Alves, who have shared tremendous vision and guidance throughout my entire time with this project.

THIS PAGE INTENTIONALLY LEFT BLANK

I. INTRODUCTION

A. BACKGROUND

1. The *Ormia Ochracea* Fly

The *Ormia Ochracea* fly developed a way to find crickets to maintain the survival of its species. The fly uses direction finding (DF) capabilities to locate a cricket that chirps at about 4.8 kHz frequency, subsequently laying its eggs on the cricket [1]. The wavelength of the cricket chirp is roughly 7 cm, and the width of the fly's hearing system is close to 1.5 mm [1]. The wavelength of the chirp is almost 50 times greater than that of the fly's hearing system, making the fly's ability to use DF to locate this chirp very intriguing.

Starting in the 1770s, with the work of J.B. Venturi, and continuing with Lord Rayleigh in the early 1900s, research has confirmed that humans use a multitude of functions and processes to have DF capabilities while hearing different sounds. The primary two components used to DF are the principles of inter-aural time difference (ITD) and inter-aural level difference (ILD) [2]. ITD occurs with animals that have a large separation between their ears with respect to the wavelength of the sound being heard. The difference in horizontal space between the ears and the wavelength of the sound causes a time difference in arrival of the sound wave between the two ears. This time difference helps the brain understand which direction the sound is coming from [2]. ILD relies on the amplitude difference caused by the phase difference which further helps identify direction of the sound. Using ILD and ITD, humans can use DF capabilities to locate sound with about 2 degrees of accuracy [2].

The question was how the *Ormia Ochracea* fly could directionally find these crickets with such accuracy without the use of ITD and ILD? [2]. After dissecting the fly and evaluating its hearing system, it was discovered that the fly had coupled eardrums that resonate two dominant modes. The ear drum can be modeled as two solid bars with a flexible hinge in between (see Figure 1) [1]. The miniscule pressure difference between the two ears of the fly creates a "rocking" mode between the bars, where the bars move out of phase with each other. The other excited resonance, the “bending” mode, is when the bars move in phase [3]. The fly uses the coupling of these two modes, which are excited by the cricket chirp, to DF and lay its eggs.

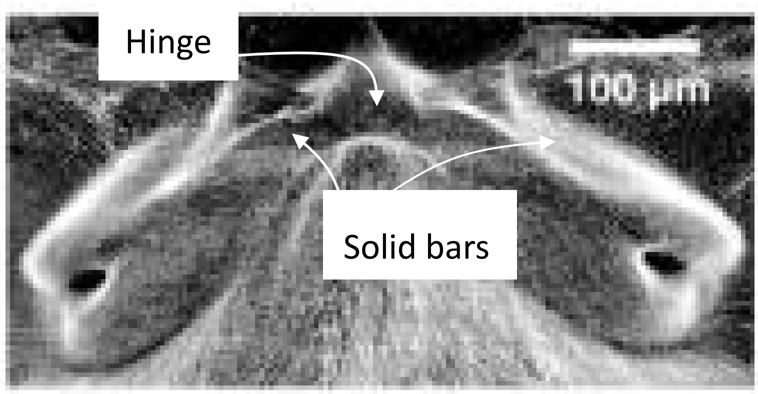

Figure 1. *Ormia Ochracea* Fly Hearing System. Source: [1].

The “bending” mode (see Figure 2) is created by the full force of the sound pressure arriving at the fly, whereas the “rocking” mode is created by the small difference in pressures received at each “bar” or eardrum of the hearing system, as previously mentioned. The “bending” mode has a higher amplitude of motion because it uses the full force of the pressure from the incident wave [4].

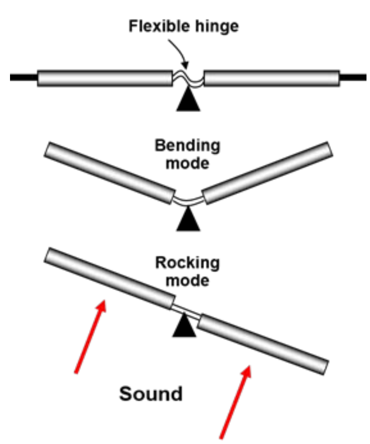

Figure 2. *Ormia Ochracea* Hearing System “Modes.” Source: [2].

Several MEMS devices have been designed into recreating a sensor to mimic the *Ormia Ochracea* hearing system. Most of these sensors spectral responses are narrowband and have capacitive combs on the wings, or use piezoelectric pads to provide electrical readout [2].

2. Initial MEMS Sensor Designs

At the Naval Postgraduate School (NPS), MEMS sensors have been researched in the past 10 years ranging from proof-of-concept [3] to high end functionality [2]. A solid knowledge has been gained allowing the design of sensors that exhibit high sensitivity in virtually any desired audio frequency.

The design shown in Figure 3 illustrates one of the first sensors fabricated and reported in *Applied Physics Letter* [3]. The sensor design includes a solid bridge with two wings extruding from each side. On each wing, there are combs that interdigitate with combs attached to the substrate. The substrate and wings are designed from single crystal silicon and the substrate is trenched away under the wings, leaving the wings free to move. Under sound excitation, the wings pivoted at the middle of the mechanical bridge oscillate similar to the *Ormia Ochracea*'s hearing system shown in Figure 2. The wings' movement, due to acoustic pressure, cause a varying capacitive output, as the comb fingers move in relation to the comb fingers on the substrate. The difference in capacitance is read by standard electronics and an output voltage, proportional to the wings oscillation amplitude is obtained.

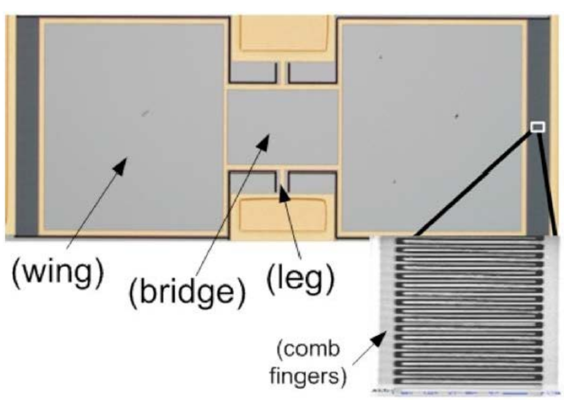

Figure 3. Early MEMS Sensor Design for In-Air Use. Source: [3].

The sensor shown in Figure 3 and all follow-on sensors were fabricated at MEMSCAP inc., a MEMS foundry that specializes in Silicon-on-Insulator Multi User Manufacturing Process (SOIMUMPS) [4].

The main characteristic of all *Ormia*-based MEMS sensors is the cosine dependence of oscillation amplitude with the angle of incidence of sound wave. This can be explained by taking into account of interaction of the sound wave with the front and back of the sensor wings [3]. The phase difference at the front and back creates a pressure gradient that is dependent on the direction of the incident wave. The low oscillation amplitude of the “rocking” mode lead to the development of directional sensors relying exclusively on the “bending” mode [4], [5]. The success of the *Ormia*-based MEMS sensors and the high interest in exploring the characteristics of such sensors underwater, motivated a new line of research, initiated by our research group, and the first results can be seen in Swan’s thesis work [5].

B. APPLICATION FOR UNDERWATER MEMS DIRECTIONAL FINDING SENSOR

The first generation of the MEMS underwater sensor, including the substrate itself, is roughly 50 mm^2. A narrowband threat detector of this size that can locate a specific tonal bearing with high accuracy would be extremely beneficial to creating an advantage in the undersea domain. This sensor, after being fully characterized and developed, could be used to operate on a submarine or surface vessel’s hull to help resolve bearing ambiguity of a contact that is being tracked on other narrowband sensors. The size of the sensor would allow it to be used on autonomous vehicles (AUVs) of all sizes, to serve as part of tracking and processing contacts. This could allow the AUV to serve as a secondary queuing source to other assets by transmitting real time bearing updates of the contacts and tonals being tracked. The possibilities for use of a sensor this size with DF capabilities are numerous, and it is vital in the future development of underwater sensors.

C. GOALS AND THESIS ORGANIZATION

The goal for this thesis work was to fully characterize a single wing underwater sensor, first introduced by Swan [5]. The results will be used to feedback the design methods and improve the next generations of sensors. In order to accomplish this objective, the sensors were fully simulated and measured in air and underwater. The thesis is organized in six chapters:

Chapter I introduces the *Ormia Ochracea* hearing system and the genesis of the *Ormia*-based MEMS sensor with DF capabilities. The potential for naval applications are also highlighted.

Chapter II presents the two designs of the generation 1 underwater sensor being characterized in air, and how each was created and simulated using the multiphysics finite element simulator, COMSOL. The chapter also compares the sensor's simulated results in air, with characterization done using the anechoic chamber and scanning laser vibrometry.

Chapter III describes the origins and changes made to the underwater sensor's mount and design employed for underwater testing. In addition, comparison of simulations of the sensors in water to actual testing in the NPS tank, as well as discusses testing attempts at Naval Undersea Warfare Center in Newport, Rhode Island are incorporated.

Chapter IV discusses the evaluation of effects of residual stress of the Generation 1 underwater sensor during the fabrication.

Chapter V introduces two new sensors that are designed to optimize sensitivity and be better suited for underwater use compared to the Generation 1 sensor. This chapter also presents initial air and underwater characterization of the new sensor.

Chapter VI assesses the results and delves into recommended follow-on work for future development of the underwater sensors.

THIS PAGE INTENTIONALLY LEFT BLANK

II. GENERATION 1 UNDERWATER MEMS SENSOR DEVELOPMENT AND CHARACTERIZATION IN AIR

A single wing sensor was designed for underwater operation. The schematic of the sensor is shown in Figure 4.

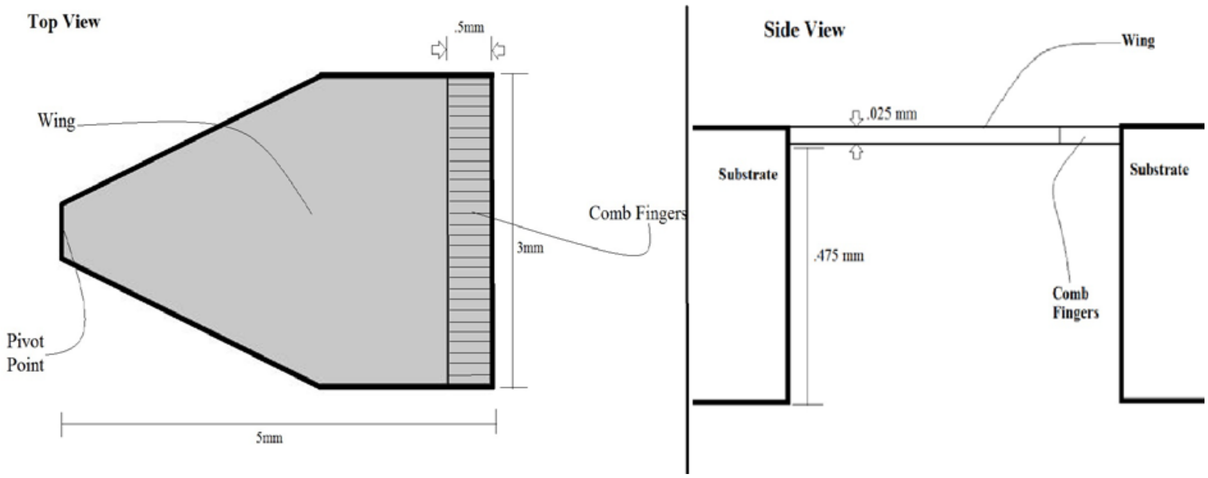

Figure 4. Schematic Top View and Side View of the Single Wing Underwater Sensor

The sensor consists of a trapezoidal wing attached to the substrate on a pivot point. The comb fingers for electronic readout of signal are located at the far end of the sensor. The sensor is made using 25 µm thick silicon (device layer) and the substrate is 500 µm thick. The single wing only allows for the "bending" mode, described in Figure 2. Since the readout relies on the capacitance of the comb fingers, the device layer is heavily doped allowing good conductivity. To operate underwater, the sensor must be immersed in a non-conductive fluid with an acoustic impedance close to water and isolated from surrounding water using a flexible boot. Silicone oil (PSF-2cST) is a good candidate, and it was used in our assemblies as discussed in Chapter III. In order to reduce the damping caused by the fluid on the comb fingers, the separation between them must be higher than that of the air operated MEMS sensors. Therefore, two configurations were designed with 5- and 10-µm gaps, respectively.

These two sensors were first designed using COMSOL finite element simulation. Once the desired response was obtained, the layouts of the sensors were done using L-Edit software and sent out for fabrication at MEMSCAP. The fabricated sensors were mounted on a printed circuit board (PCB) and wire bonded for extracting electrical output. The sensor was characterized in an anechoic chamber and using laser vibrometry. The results from the COMSOL simulation, anechoic chamber and the laser vibrometry were compared and analyzed before the sensor was further characterized in the underwater environment. The results, in future work, will be used to refine the simulation models and adjust the next generation of sensor characteristics as desired.

A. SENSOR DESIGN AND SIMULATION

1. COMSOL Design of Generation 1 MEMS Underwater Sensor

All the MEMS DF sensors (air and underwater) are first designed in COMSOL and simulated before being manufactured and tested. COMSOL Multiphysics is a sophisticated finite element modeling and simulation tool that integrates all relevant phenomena. This allows the design of different sensors and different environments and external stimuli needed, whether that be sound, thermal or electrical. The basic layout for sensor design is straightforward. First, the sensor structure is designed in 2D. This can be simplified in COMSOL, since the sensor is symmetrical along the length of the sensor, and only one half of it needs to be drawn.

Once a 2D drawing is complete, it can be extruded to take its 3D form. A damping expression is inserted as a boundary load condition where the combs would be located, allowing the simulation to take place as if the comb fingers were there. The equation can easily be modified to consider a 5- or 10-micron gap between fingers. How this damping equation is entered and its effects on the COMSOL simulation are discussed in Part D of this chapter. After the geometry is completed, material properties are assigned to each specific part of the sensor and the environment. To simulate the sensor in air, it will just use air as the surrounding material; to simulate the sensor for underwater operation, silicone oil (PSF-2cST) was used for the surrounding material.

The accuracy of the material properties of the sensor components is very important. Ensuring that they are the same as those of materials used to manufacture the sensor enhances the reliability of the simulation results. This initially caused a concern due to the variability of Young's modulus and elasticity properties of silicon. Silicon's Young's modulus can vary up to 45% based on the orientation of the crystal lattice structure in the silicon [6]. If the Young's modulus differs in the simulation to that of the manufactured sensor, results could also differ dramatically. The Young's modulus or elastic modulus is a value that quantifies the elastic behavior of the material [6]. However, since single crystal silicon is not an isotropic material, use of a single elastic constant does not provide accurate results. Thus, it is necessary to treat silicon as an anisotropic material and employ appropriate stress tensor in COMSOL. The values for this tensor can be found in material text books if the correct crystal orientation of the sensor structure used in fabrication is known. The most commonly used orthotropic elasticity matrix for silicon is based on [100], [010], and [001] as the principal axes [6]. However, SOIMUMPS process uses [110], [110], and [001] as the principal orientations [6]. The structure of the referencing of the directions of the crystal lattice is described in detail in a paper by Hopcroft [6]. The normal anisotropic elasticity matrix for silicon is a 6x6 matrix of elastic constant components (C), but due to the symmetries of the crystal structure of silicon it reduces to 21 independent values. These values are shown in Table 1.

Table 1. Elasticity of Anisotropic Silicon Used to Create Sensor, Values in GPa. Source: [6].

194.5 (C_{11})	35.7 ($C_{12/21}$)	194.5 (C_{22})	64.1 ($C_{13/31}$)	64.1 ($C_{23/32}$)	165.7 (C_{33})	0 ($C_{34/43}$)
0 ($C_{35/53}$)	0 ($C_{36/63}$)	79.6 (C_{44})	0 ($C_{41/14}$)	0 ($C_{42/24}$)	0 ($C_{45/54}$)	0 ($C_{46/64}$)
79.6 (C_{55})	0 ($C_{51/15}$)	0 ($C_{52/25}$)	0 ($C_{56/65}$)	0 ($C_{61/16}$)	0 ($C_{62/26}$)	50.9 (C_{66})

Next, the equations to be solved are selected through the physics, interactions and boundaries placed on the model. Figure 5 shows the basic sensor geometry with the applied boundaries and excitation fields. Meshing allows the simulation to take place by breaking up the areas of the model into discrete shapes. The meshing process can be challenging in COMSOL based on the size of some of the features.

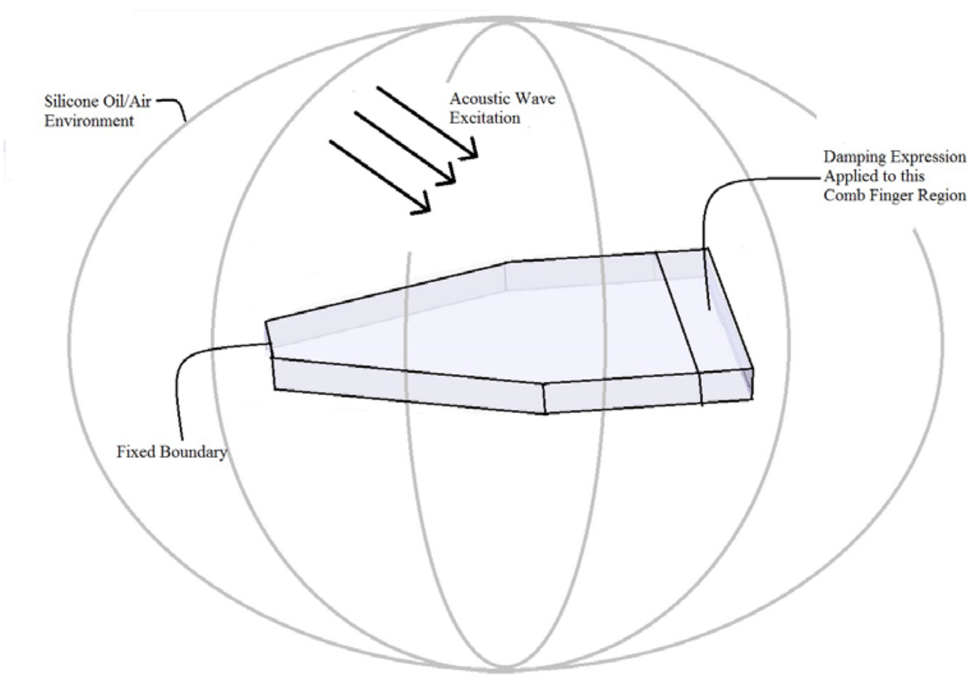

Figure 5. Basic 3D Sensor Example with Boundaries, Excitation and Environment

2. COMSOL Simulations

Two studies were performed on the modeled 5- and 10-micron gap sensors. The first study simulates a plane wave incident in the normal axis of the sensor. The wave sweeps a range of frequencies. This is to determine the resonance frequency of the “bending” mode. A convenient feature in COMSOL is that due to the symmetry along the wing of the sensor you only need to perform the test on one half of the sensor using a symmetry boundary condition. This allows computation time to be much shorter. Figure 6 shows a 3D simulation of the sensor subjected to a normal incident acoustic plane wave on just the sensor wing and not the substrate.

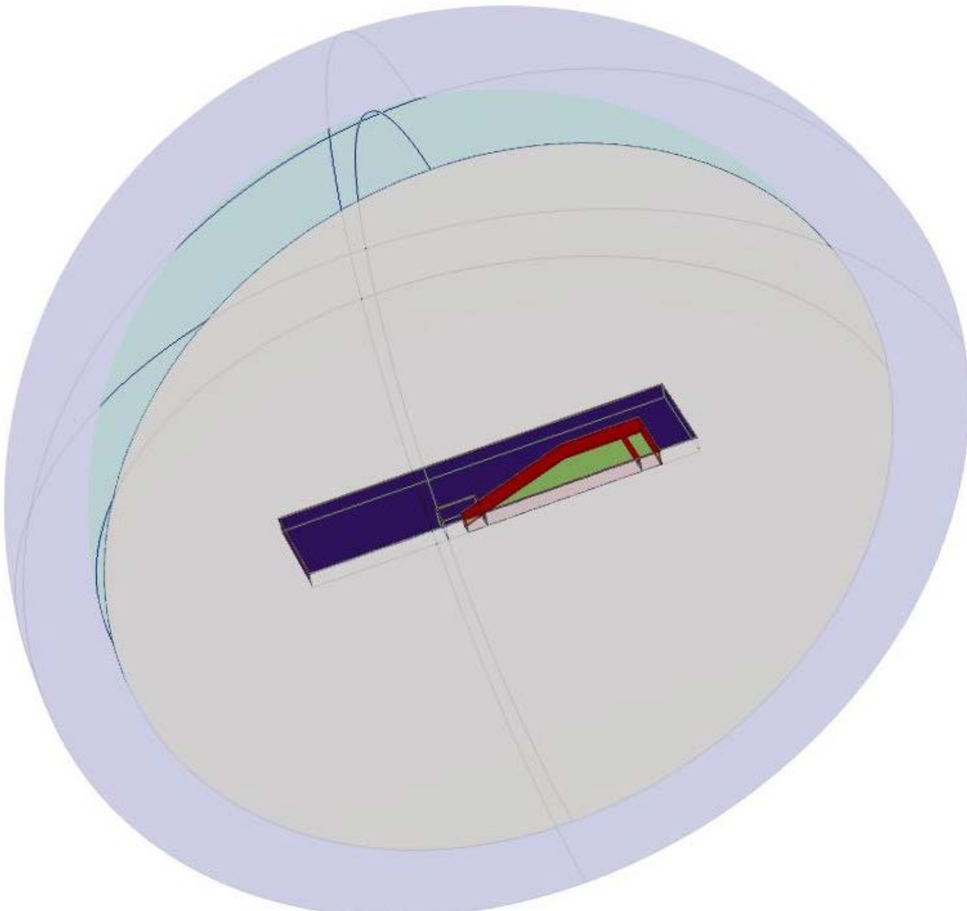

The 3D simulation represents the result of a normal incident sound wave and the resulting total acoustic pressure field on the sensor. The dark red regions represent the highest amount of pressure. The green is less pressure, and dark blue represents no pressure on the area (substrate). The spheres around the sensor are the environment boundaries and are the limits of where the sound wave can operate.

Figure 6. COMSOL 3D Simulation of a Normal Incident Sound Wave

The second simulation performed on each sensor by varying the angle of incidence of the sound wave while keeping frequency at the “bending” resonant frequency found in the first simulation. The frequency response results are shown in Figure 7 for the 10- and 5-micron gap sensors. The peak of the graph represents the maximum displacement amplitude measured at the tip of the sensor and the corresponding resonance frequency of the “bending” mode.

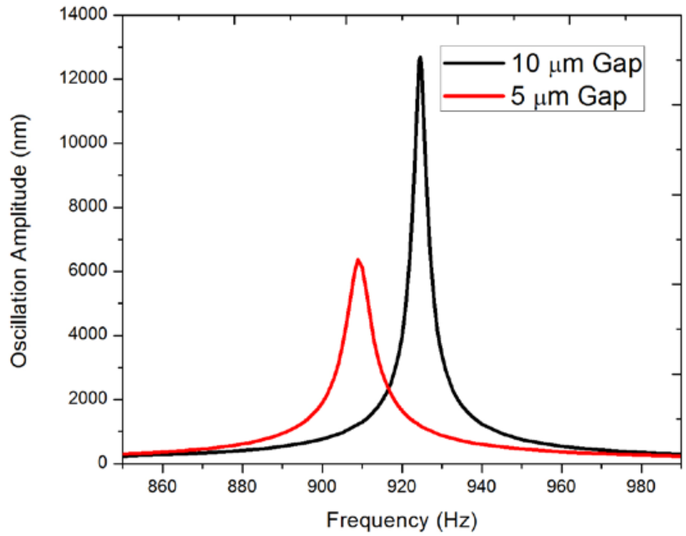

Figure 7. COMSOL Simulation of 10- and 5-Micron MEMS Sensors with Normal Incident Wave, Frequency Sweep 800–1000 Hz

Figure 8 shows the second simulation performed on each sensor. The peak frequency of the previous simulation was chosen for the plane wave to operate at for the rotation test which was 10-micron sensor (924 Hz) and the 5-micron sensor (910 Hz). The incidence angle of the sound wave is rotated from -180 degrees to 180 degrees.

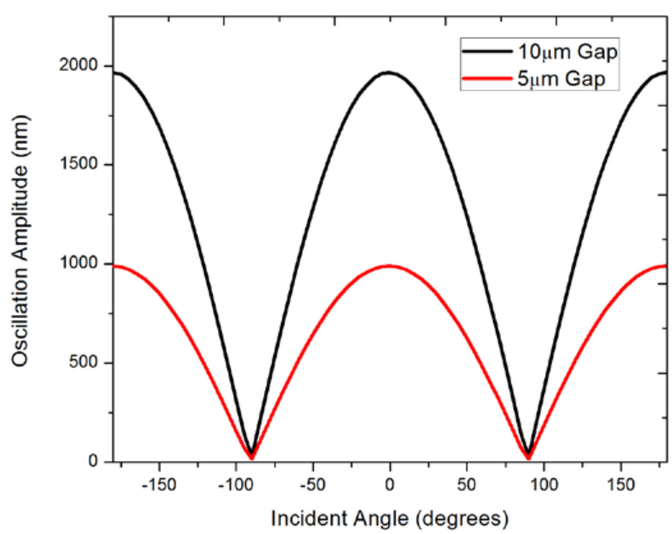

Wave is produced at 924 Hz for the 10-micron and 910 Hz for the 5-micron. The black line represents the 10-micron sensor incident angle rotation with a sound wave at 924 Hz and the red line represents the 5-micron sensor with a sound wave at 910Hz.

Figure 8. COMSOL Simulation 10- and 5-Micron MEMs Sensor Changing Incident Angle of the Sound Wave

Figures 7 shows a narrowband response peaked at 924 Hz for the 10 -micron sensor and 910 Hz for the 5-micron sensor. The resonance frequency peak is lower for the 5-micron sensor due to the more mass created from having more comb fingers. Figure 8 shows the directional dependence of the sensor response when operated at near the "bending" mode resonance frequency. The response shows a maximum at normal incidence (head-on) and a minimum at 90 degrees (directly to one side), with a sinusoidal dependence. Figure 8 also shows that both sensors exhibit a similar directional response with the 10-micron sensor having a higher oscillation amplitude due to the lower damping of the comb fingers.

B. GENERATION 1 UNDERWATER SENSOR FABRICATION AND TESTING IN AIR

1. Sensor Fabrication

The 5- and 10-micron sensors were both fabricated at MEMSCAP Inc. foundry using their proprietary SOIMUMPS technology. A picture of a fabricated 10-micron sensor is shown in Figure 9.

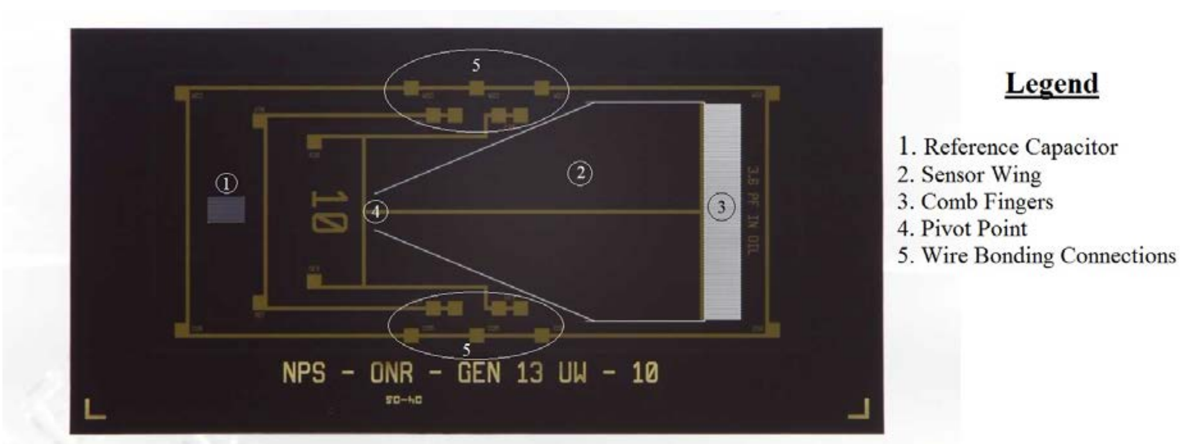

Figure 9. Fabricated 10-Micron Sensor and Key Components

This fabrication process is the same for the two-winged air sensors used in previous work [3]–[5]. To convert the wing displacement into electrical output, a universal capacitive readout integrated circuit (MS3110) was used [7]. The sensor and integrated circuit were placed on a PCB that allows for programming, bias and output readout, while providing physical support for sensor testing and characterization. The MEMS sensor electrical output relies on the capacitance difference between the comb finger capacitor and the reference capacitor (Figure 9). The sensor was wire bonded to the PCB with 25-micron diameter gold wire. The MS3110 Integrated Circuit was programmed using a developmental board, and the sensor and reference capacitors were balanced to provide 2.5 V output with no sound stimulus. The fully configured sensors are shown in Figure 10.

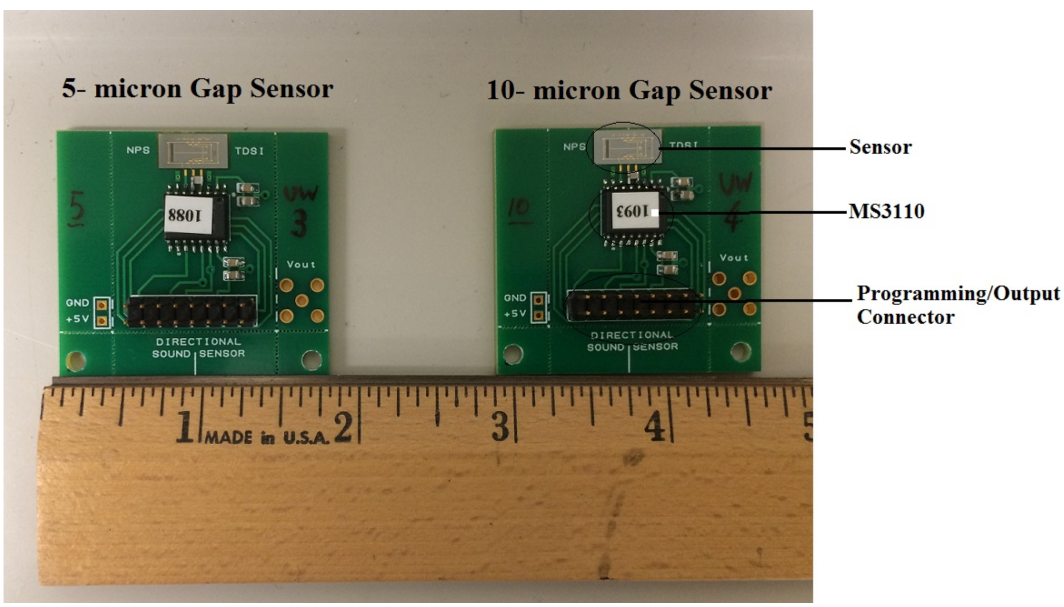

Figure 10. Picture of Both 5-Micron and 10-Micron Sensors Assembled on their Respective PCBs

2. Sensor Characterization in Anechoic Chamber

Frequency response, directional response and sensitivity were measured for both sensors in the acoustic anechoic chamber at NPS.

The sound source was a JL Audio 6-inch speaker which was connected to sign wave output of a SR865 lock-in amplifier via a HP467A power amplifier. The sensor was mounted to the B&K Type 5997 turntable controller that attaches to the ceiling of the anechoic chamber. The lock-in amplifier supplies 5 Vdc through its aux output to the sensor electronics, and the sensor response was routed back to the lock-in amplifier which showed the results on a touch screen display real time. The set-up of the anechoic chamber is shown in Figure 11. Figure 12 shows a block diagram of the assembly, and Figure 13 shows the displays and controls.

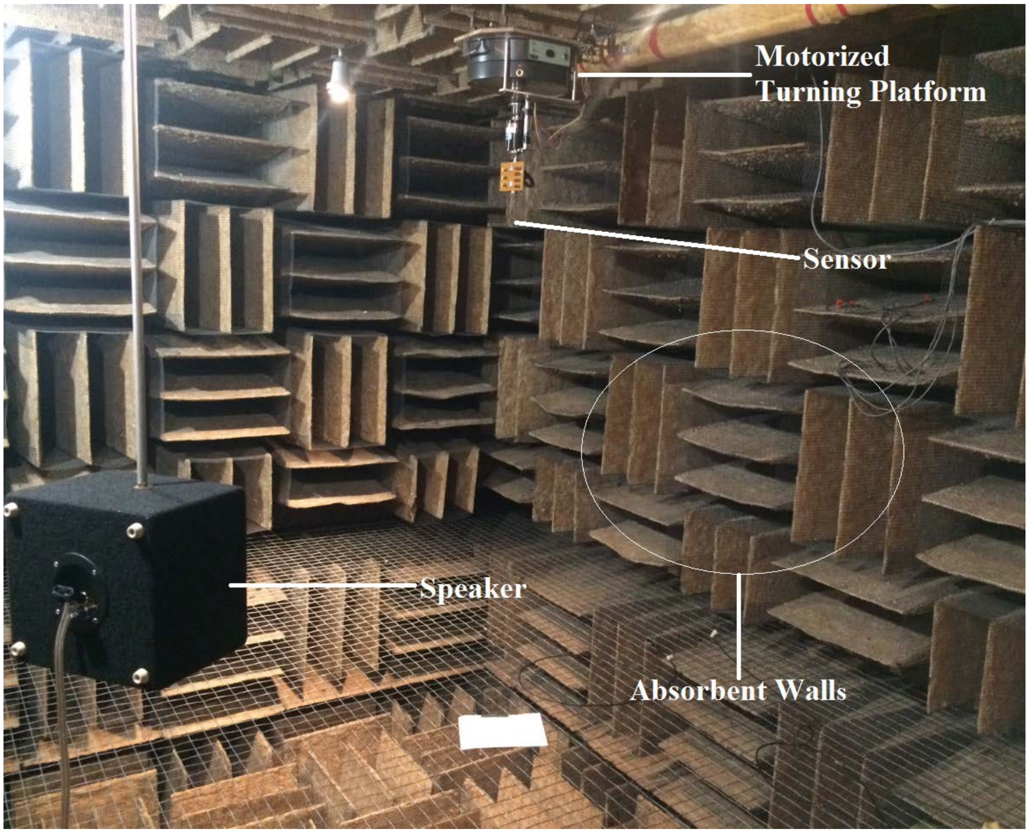

Figure 11. Anechoic Chamber Setup for Testing

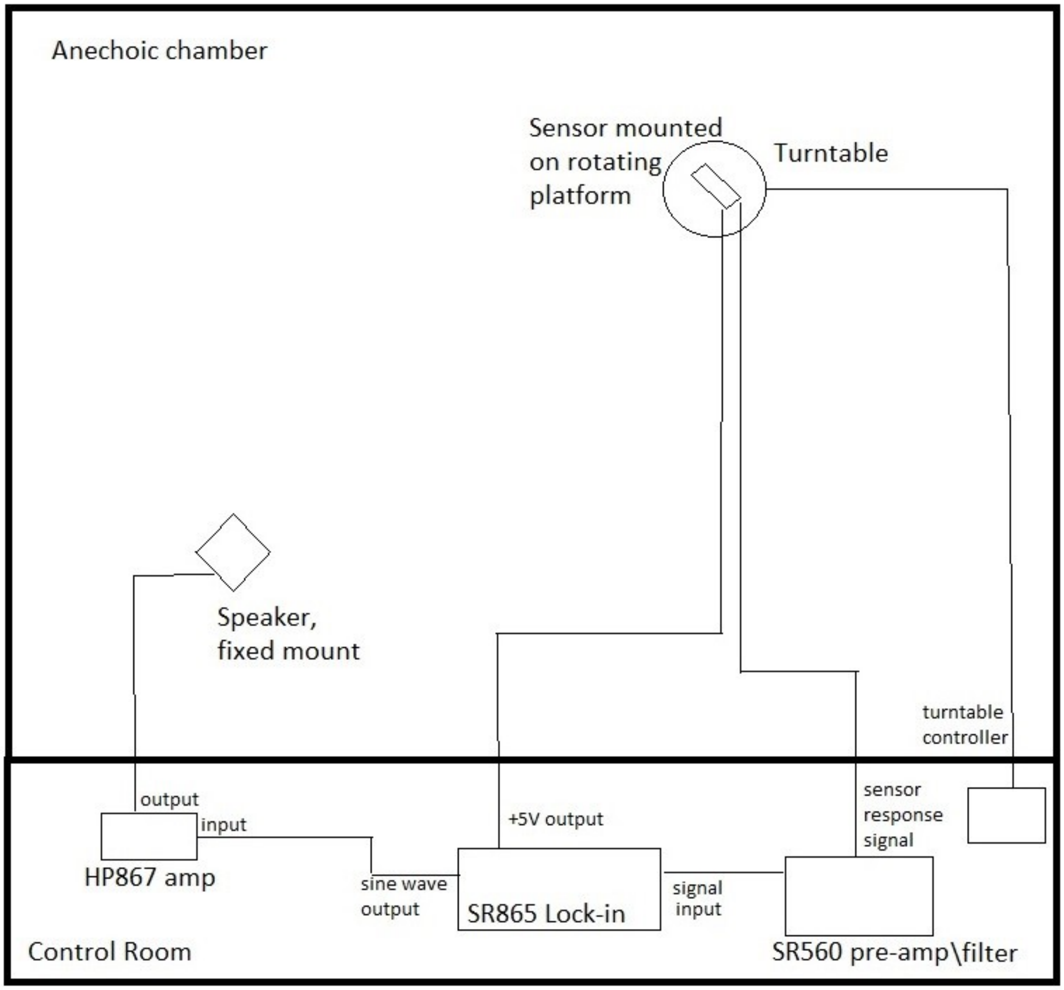

Figure 12. Block Diagram of Anechoic Chamber Testing. Source: [5].

The figure shows the set-up and controls for performing the tests in the anechoic chamber. 1. SR865 lock-in amplifier 2. B&K Type 5997 turntable controls 3. Back-up HP467A power amplifier 4. Multimeter 5. HP467A power amplifier.

Figure 13. Instrumentation Used in the Anechoic Chamber Testing

a. Frequency Sweep

The speaker was mounted approximately 12 feet from the sensor, which was sufficient to achieve far-field for the frequencies used. The sound source was driven at 2 V peak for all frequencies from 500 Hz to 1300 Hz in 100 seconds. The results were recorded. Both sensors showed strong “bending” mode resonant peaks with narrow bandwidths.

Figure 14 shows the results of the 10-micron and 5-micron frequency sweep tests, respectively.

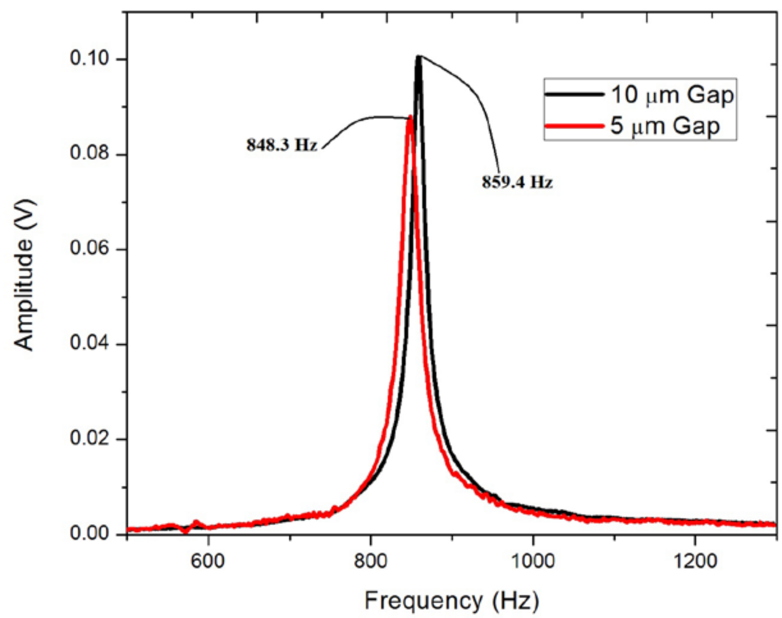

Figure 14. 5- and 10-Micron Sensor Frequency Sweep Test, Normal Incidence, 500–1300Hz, Sound Pressure at Sensor 22.1 mPa

As shown in Figure 14, the peak frequency of the 10-micron sensor is 859 Hz and the peak frequency for the 5-micron sensor is 848 Hz. The shape of each curve was similar to that of the COMSOL simulation, but both sensors saw changes in the peaks positions. The 10-micron decreased from 924 Hz to 859, and the 5-micron sensor from 909 Hz to 848 Hz. This can be attributed mostly to the manufacturing process of the sensors. The design thickness of 25 microns may fluctuate up or down by a micron, and the change in weight will cause a slight shift in the resonance frequency. The trenching process utilized in the SOIMUMPS process can generate an undercut making the pivot point different from that of the simulation which assumes it to be at the exact boundary (shown in Figure 5). However, in the actual sensor the pivot point could be further down the wing. This change in the pivot point would affect the resonance frequency. To explore the effect of thickness on the resonant frequency, the 10-micron sensor was re-simulated for a 26 micron thick wing, and the results were compared with the original simulation. Figure 15 shows the comparison between the new simulation and the old simulation and how much the change in thickness by one micron effects the resonance peak.

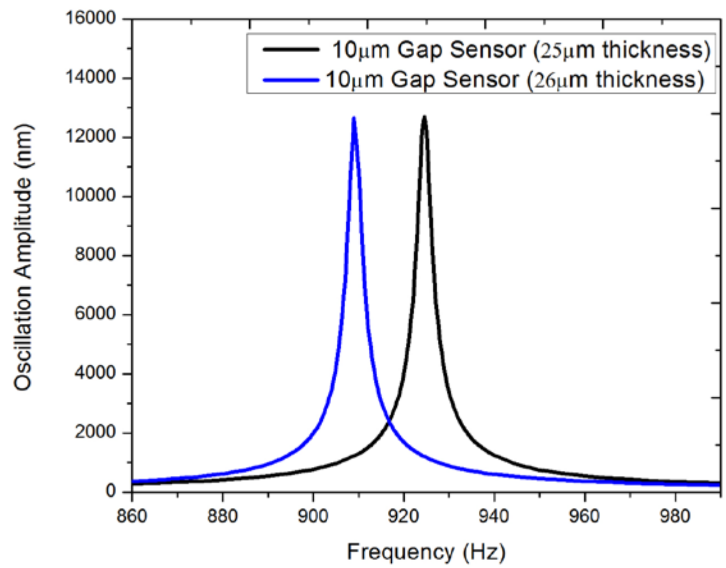

Figure 15. COMSOL Simulation of Normal Incidence Wave Showing Change in Resonance Peak Due to Change in Thickness Parameters

b. Incident Angle Rotation

For the second test, the set-up was the same. The mounted sensor was rotated from normal incidence (0 degrees) to 360 degrees in 120 seconds. The sound source was operating at the "bending" mode resonance frequency that was found during the frequency sweep test. This rotation of the sensor changes the incident angle of the sound wave on it. The results from the incident angle test can be seen in Figures 16 and 17 for the two sensors.

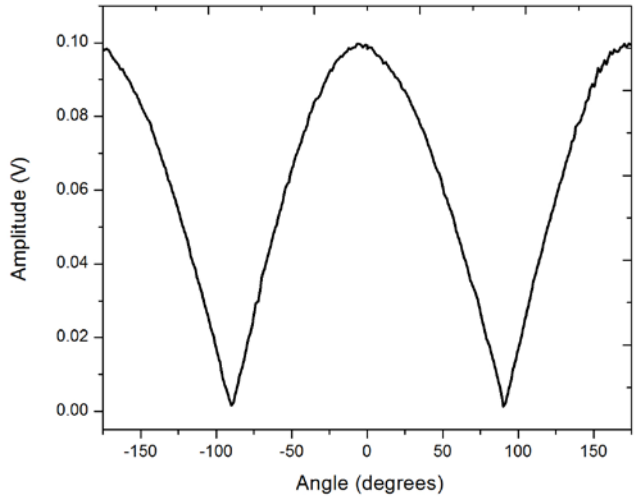

Figure 16. 10-Micron Sensor, Directional Response at 859 Hz, Sound Pressure at Sensor 22 mPa

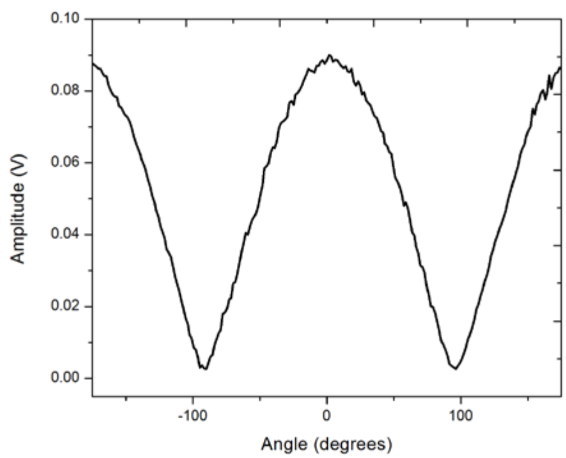

Figure 17. 5-Micron Sensor, Directional Response at 848 Hz, Sound Pressure at Sensor 22 mPa

Figures 16 and 17 show the expected cosine dependence to angle of arrival as seen in the simulations. The only difference between these experimental results and the COMSOL simulations is that the 5-micron showed a stronger voltage output response than expected from the simulations. These sensors have shown the ability to be DF capable in air as expected.

c. Sensitivity Analysis

The sensitivity of the sensors was measured by means of output voltage per sound pressure level. It is important to notice that it is dependent on gain, programmed into the MS3110 universal readout. To assume a fair comparison, the MS3110 of each sensor was programmed to balance the sensors' capacitances using the same gain parameters (as shown in Appendix E and F). The sound pressure level was obtained using a G.R.A.S. Free Field Microphone Type 40 AF mounted at the same distance from the speaker as the sensors. The microphone's sensitivity is 45.3 mV/Pa and is extremely linear in the region we operated in [8]. A series of six measurements of the microphone and the sensors were taken while increasing the voltage of the output speaker. The voltage of the received signal from the microphone, the sensitivity of the microphone and the received voltage of the sensor yielded the following results for the 10-micron sensor in Table 2 and the 5- micron sensor in Table 3.

Table 2. Sensitivity Measurement of 10-Micron MEMS Sensor Tested in Air

Speaker Output (V_{rms})	Reference Microphone (mV)	Sound Pressure at Sensor (mPa)	10-Micron MEMs Underwater Sensor output (mV)	10-Micron MEMs Sensor Sensitivity at 859.4 Hz (V/Pa)
0.5	0.27	5.96	26.1	4.38
1	0.53	11.70	50.7	4.33
2	1.03	22.74	98.6	4.34
4	2.03	44.81	191.23	4.27
10	4.79	105.74	458.2	4.33
20	9.00	198.68	870.6	4.38

Table 3. Sensitivity Measurement of 5-Micron MEMS Sensor Tested in Air

Speaker Output (V_{rms})	Reference Microphone (mV)	Sound Pressure at Sensor (mPa)	5-Micron MEMs Underwater Sensor output (mV)	5-Micron MEMs Sensor Sensitivity at 848.3 Hz (V/Pa)
0.5	0.27	5.96	19.7	3.31
1	.53	11.70	42.5	3.63
2	1.03	22.74	88.40	3.88
4	2.03	44.81	169.90	3.80
10	4.79	105.74	369.91	3.50
20	9.00	198.68	610.10	3.07

The sensitivity of the 10-micron sensor is approximately 4.34 V/Pa and the 5-micron sensor output is approximately between 3.62 V/Pa. The outlier reading for the 5-micron sensor at 20 Volt speaker output was left out of the average. The 5-micron sensor showed more fluctuations in sensitivity based on the output voltage, but overall, both sensitivity tests showed reasonable consistency throughout all levels.

C. LASER VIBROMETRY

To confirm the location of the resonance peak of the sensors and to further analyze the reaction of the sensor when presented to a frequency sweep, each sensor was tested using a scanning laser vibrometer at the Polytech Inc. laboratory in San Jose. The model used in testing was the Polytech MSA-500 micro system analyzer. A picture of the MSA-500 is shown in Figure 18.

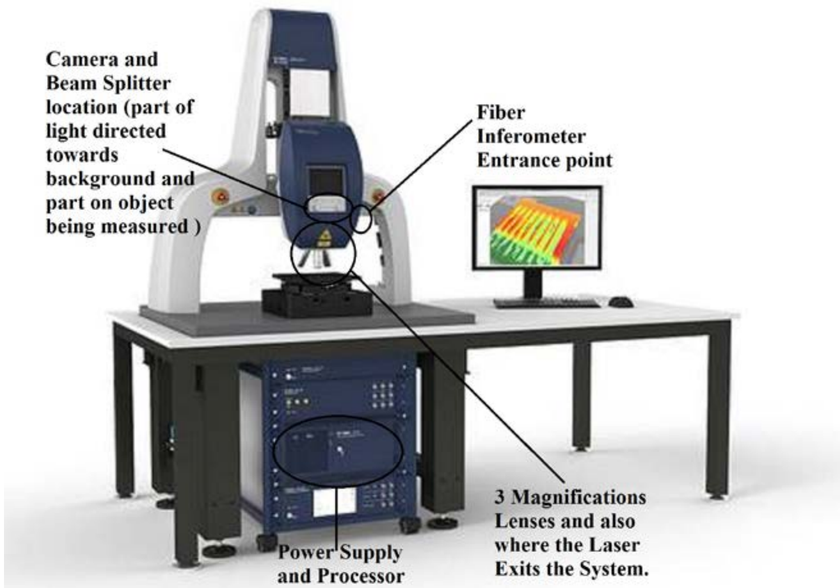

Figure 18. MSA-500 Micro System Analyzer Laser Vibrometer Used in Testing. Source: [9].

The laser vibrometer is a precision optical tool for determining the velocity and displacement at a certain position. It senses the frequency shift of backscattered light from a moving surface. The object scatters light from the laser beam, and the Doppler frequency shift allows for the velocity and displacement to be measured along the axis of the laser beam [9]. It began the analysis by placing a pin point laser at multiple spots of the sensor wing. A sound was then introduced at close to normal incidence of the sensor, and frequency of the source was swept. The laser scanning system measured the oscillation amplitude of the sensor at different locations. The measurements gave the displacement of oscillations divided by the voltage supplied by the function generator to the speaker. This test proved another method to measure the resonant peak of the sensors. The laser mapping of several points on the sensor surface is shown in Figure 19. Each number on the figure is a point on which the laser measured the oscillation of the wing. Three points which were the same distance from the pivot (left, right and middle) were graphed, and there was no discernible difference in magnitude. This lack of difference in magnitude suggests that very little torsional motion exists, and that the wing is maintaining the bending mode as expected.

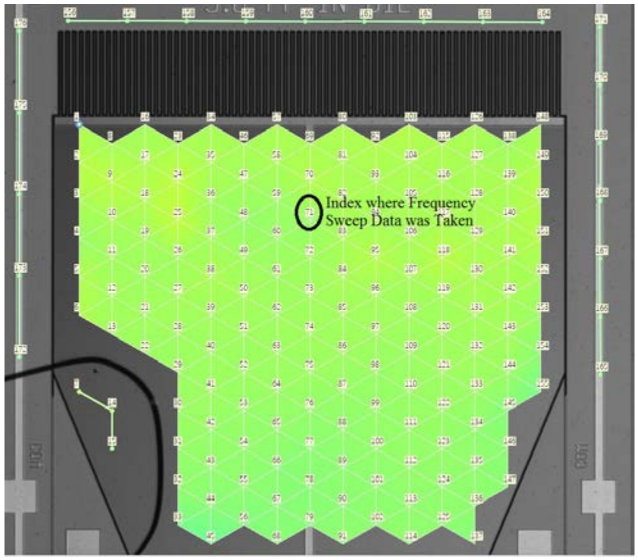

Figure 19. Indices Performed on the Sensor Wing by Laser Vibrometer

Figure 20 and Figure 21 show the frequency response of the 10-micron and 5-micron sensors. The resonant peak of the 10-micron was 859 Hz and the resonant frequency of the 5-micron sensor was 848 Hz. The graphed data in Figure 20 and 21 is taken from a point near the center of each of the sensor wings.

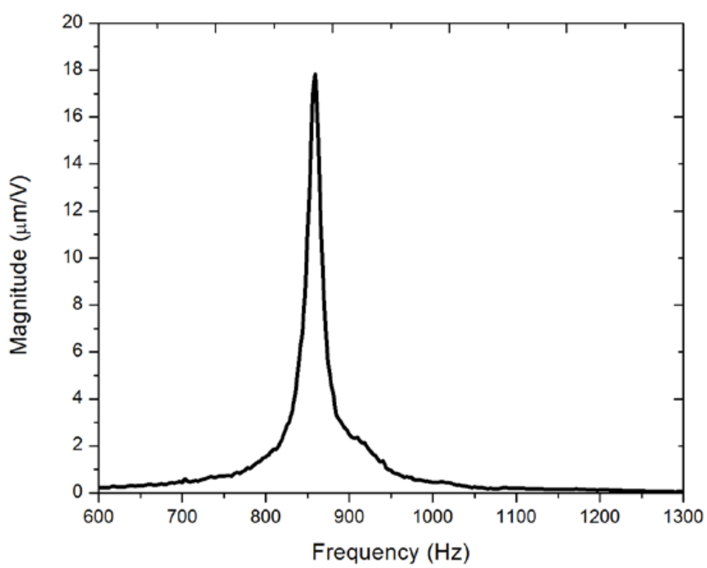

Figure 20. 10-Micron Sensor Frequency Sweep Test on Laser Vibrometer, Normal Incidence, 600–1300Hz

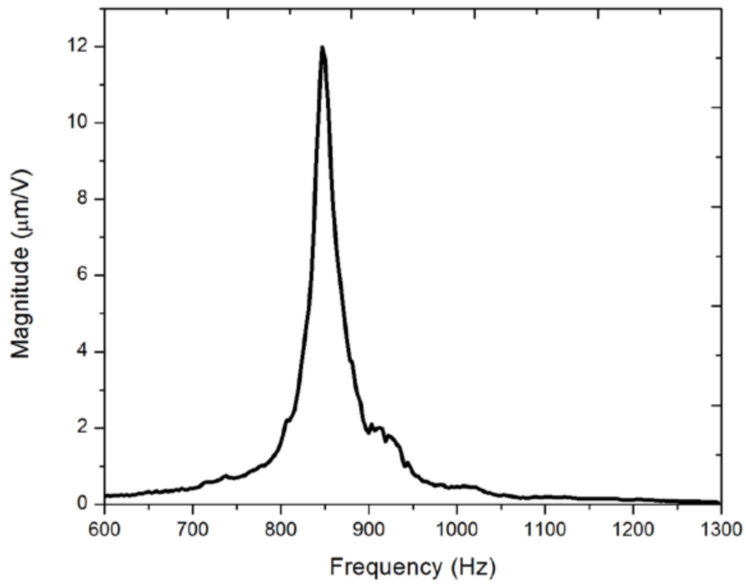

Figure 21. 5-Micron Sensor Frequency Sweep Test on Laser Vibrometer, Normal Incidence, 600–1300Hz

The results from laser vibrometer are highly comparable to that of the tests in the anechoic chamber as expected. Due to the physical limits of the laser vibrometer, an incident angle sweep could not be performed on the sensors. Based on the results from the normal incidence frequency sweep, it is expected an incident angle rotation would have very similar results to that of the anechoic chamber testing.

D. DAMPING EFFECTS

Damping Model and COMSOL Implementation

As mentioned in part B.1 of this chapter the damping and drag forces of the wing and the comb fingers needed to be input into the software as a boundary load. Work done by Klose et al. has shown that successful modeling of damping in a MEMS sensor can be broken down into two parts: the damping caused by the combs, and the damping of the wing [10]. Each of these has a governing equation that can entered in COMSOL as a "boundary" condition. For the combs the flow between them can be considered *Couette* flow, this force can be expressed by the following equation [10]:

$$F_d \approx F_{Couette} = -\eta_{eff} * \frac{A_s}{g} * \nu \tag{2.1}$$

where F_d is the drag force of the combs, η_{eff} is the dynamic viscosity, A_s is twice the overlap area of the moving and fixed comb fingers, g is the gap between combs and ν is the velocity of the movable region with respect to the medium [10]. Modeling the comb finger region in COMSOL requires the use of equation 2.1 and a calculation of the average density the combs region taking into account the air gaps. The average density can be calculated by multiplying the density of silicon, 2330 $\frac{kg}{m/s^2}$, by the fraction of combs in the region. For the 10-micron sensor this fraction is $\frac{10\ micron\ comb}{every\ 40\ microns}$ or (0.25) and $\frac{10\ micron\ comb}{every\ 30\ microns}$ or (0.33) for the 5-micron sensor. The ν is calculated by COMSOL based on the displacement of wing at the boundary in $\frac{m}{s}$, and A_s is the overlap area of the moving and fixed comb fingers. The g is either 10 or 5 microns depending on the sensor. This damping has a much smaller overall effect on simulation output. The greater damping effect comes from drag produced by the entire wing. Any object moving relative to a fluid experiences a drag force given by [10]

$$F_d = -\rho_m * \frac{A_p}{2} * \nu^2 * c_d \tag{2.2}$$

where ρ_m is the density of the silicon (2330 $\frac{kg}{m/s^2}$), A_p is the base area of the wing, and c_d is the drag coefficient, an empirical factor which can be determined by experiments or analysis [10]. The initial COMSOL simulations showed a shift in resonant peak, but also the peak width was did not correspond to that of the test run in the anechoic chamber and laser vibrometer. To calculate and empirical drag coefficient we use the quality factor (Q) of the experimental frequency response. Q is a precise way to define the sharpness or width of a resonant curve [11]. It is given by

$$Q = \frac{f_0}{(f_u - f_l)} \tag{2.3}$$

where f_0 is the resonant frequency and f_u and f_l are the two frequencies above and below in which the amplitude is one half that of the resonance value [11]. After adjusting The coefficient c_d was adjusted by trial and error comparing simulation and measurements, and it was found to be about 300. After adjusting the drag coefficient, the Q value results obtained experimentally compared with those of the COMSOL simulations are shown in Table 4.

Table 4. Quality Factor Calculations for 5- and 10-Micron Sensors in Air

	Quality Factor 10- micron Sensor	Quality Factor 5-micron Sensor
Anechoic Chamber Test	39.7	27.1
Laser Vibrometer	41.3	26.6
COMSOL Simulation, after adjusting c_d to 300, shown in Figure 22	38.3	24.4

This c_d value will be used for further simulations of the single wing underwater sensors operated in air. Figure 22 and Figure 23 compare the normalized amplitude of the two experimental measurements and the adjusted COMSOL simulation for the normal incidence sound wave frequency sweep.

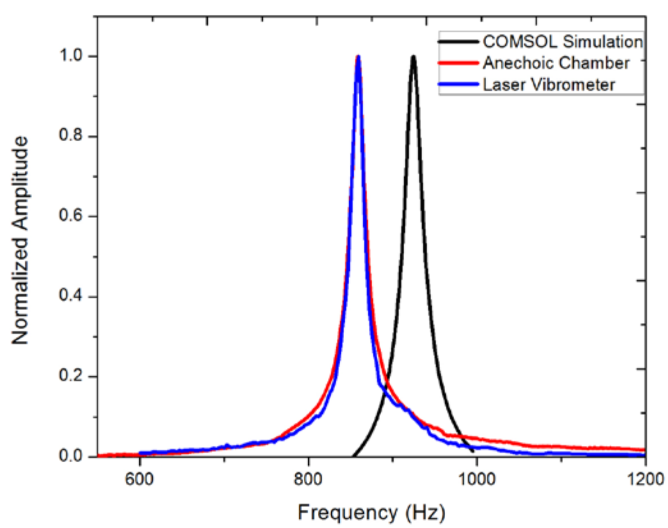

Figure 22. 10-Micron Normalized Amplitude Frequency Sweep with Adjusted c_d Parameter for Simulation

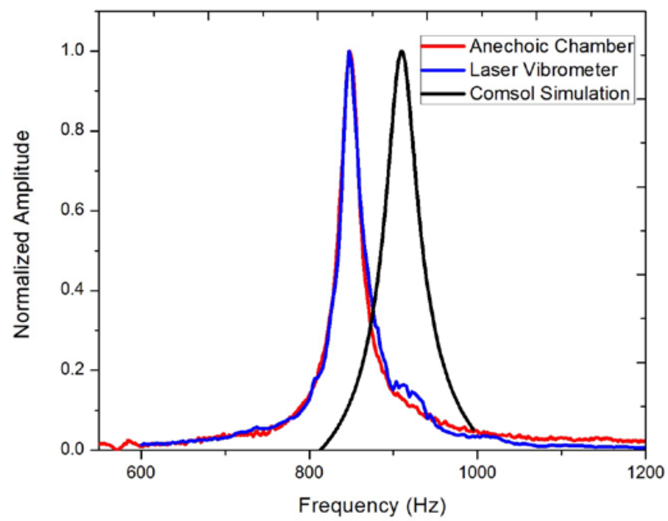

Figure 23. 10-Micron Normalized Amplitude Frequency Sweep with Adjusted c_d Parameter for Simulation

Further work is needed to determine the best way to model the drag on the MEMS sensor wing and to determine the competing drag effects on the combs versus the wing itself.

E. AIR CHARACTERIZATION AND DESIGN RECOMMENDATION

The MEMS underwater sensor design and simulation process has numerous intricacies that have not been perfected. It is important to ensure proper damping effects are incorporated in simulations based on knowledge gained by experimentation. Based on the available parameters for simulations, two single wing sensors have been successfully designed, simulated, fabricated, and characterized in air. The two sensors showed consistency in two different frequency sweep experiments; one performed with equipment in the anechoic chamber to obtain electrical output and the other using a laser vibrometer to obtain wing displacement. Each test provided consistent resonant peak positions and both showed Q values within 3.5% accuracy for the 10-micron sensor and 1.8% for the 5-micron sensor. The testing in the anechoic chamber successfully showed a cosine dependence on the angle of arrival. The 10 and 5-micron sensors programmed with the parameters described in Appendix E and F showed a sensitivity of 4.34 V/Pa and

3.62 V/Pa respectively. These results provided the necessary knowledge to proceed to the underwater characterization.

THIS PAGE INTENTIONALLY LEFT BLANK

III. UNDERWATER MEMS SENSOR ADAPTION AND CHARACTERIZATION IN WATER

The 5- and 10-micron sensors have shown strong narrowband frequency responses when tested in air. Both sensors have proven to have directional responses with a cosine dependence on the angle of incidence of sound. The next step is the characterization of the sensors in the underwater environment.

A. MOUNT AND HOUSING DEVELOPMENT FOR UNDERWATER APPLICATION

The housing and mount developed by Swan to adapt the sensor for the underwater environment [5] are used with slight modifications. The goal was to make a rubber housing with a high transmission coefficient, so that it would not affect the pressure wave incident on the sensor during testing [5]. To make this possible, the rubber housing was created out of Flexane 80 [5]. Flexane 80 has been calculated to have an impedance of $z=2.51x10^{6}\ Pa\ s/m$ [5]. The sound wavelength that will be used for the underwater characterization ranges from roughly 5–15 meters [5]. The rubber housing only has a thickness of roughly .01 meters. Using this information, it was found that the rubber mold with silicon oil fill had a transmission coefficient of .95 in water and $3.4x10^{-3}$ [5] in air. These calculations and assumptions can be found in Appendix A. The mold used to manufacture it can be seen in Figure 24.

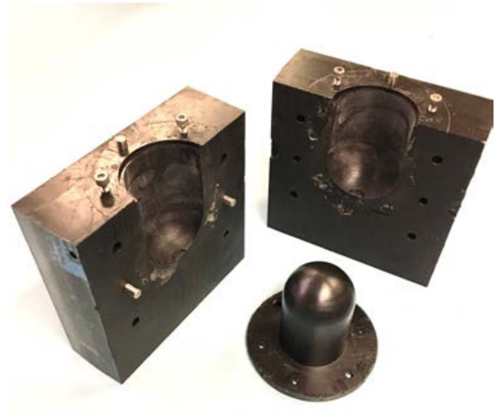

Figure 24. Mold for Manufacturing the Rubber Housing for the Underwater Operation. Source: [5].

The fluid used to fill the rubber housing needed to be non-conductive, allow for free motion of the interdigitated fingers and nearly match the impedance of water to allow for uninterrupted wave travel [5]. PSF-2cST silicon oil was found to have the required characteristics and was used in the experiments. Three rubber housings were manufactured to make additional fully assembled underwater sensors. The former three-part mount assembly made by Swan [5] was mated and a one-piece mount made of stainless steel with a stainless-steel O-ring were manufactured. The three parts that make up the entire assembly (reduced from five parts previously) is shown in Figure 25.

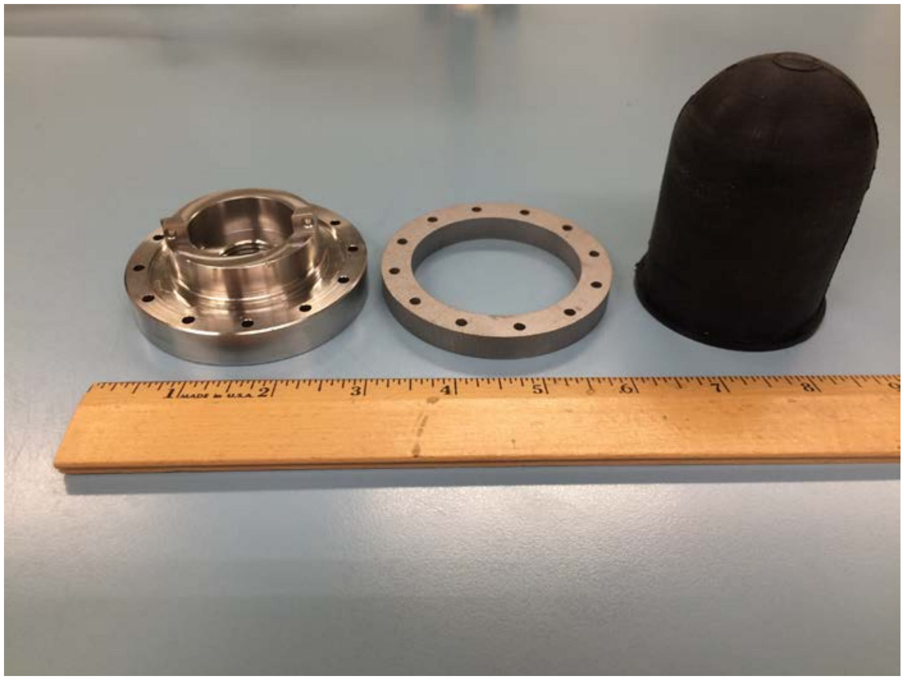

Figure 25. The Sensor Mount Made of Stainless Steel, 12-Hole Stainless Steel Ring to Seal Housing and Mount, and Flexane-80 Rubber Housing (left to right)

A 12-pin mini link connector was placed into the bottom of the sensor mount and epoxy was used to create a water seal. The 12-pin cables were then soldered to a 16-pin ribbon cable that was liquid taped to water seal the assembly again. The connections of the ribbon cable to the pins is in Appendix C, and pictures of the soldering of the mini-link to the 16-pin ribbon prior to sealing can be seen in Appendix D. Once this is complete the sensor on the PCB is mounted as shown in Figure 26.

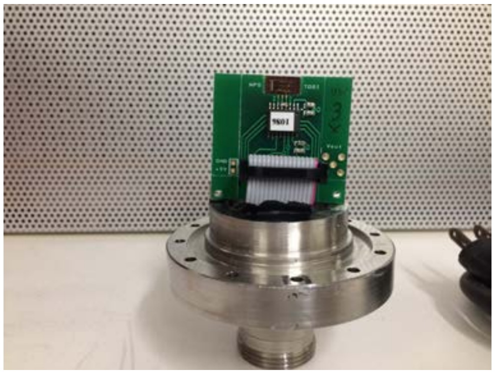

Figure 26. Sensor Screwed to Mount and Attached to12-Pin Ribbon Cable

A ribbon cable was spliced with a transmission cable that ended with a connector that matches the mount. This allowed for programming the MS3110 when the full assembly is completed. This cable is shown in Figure 27.

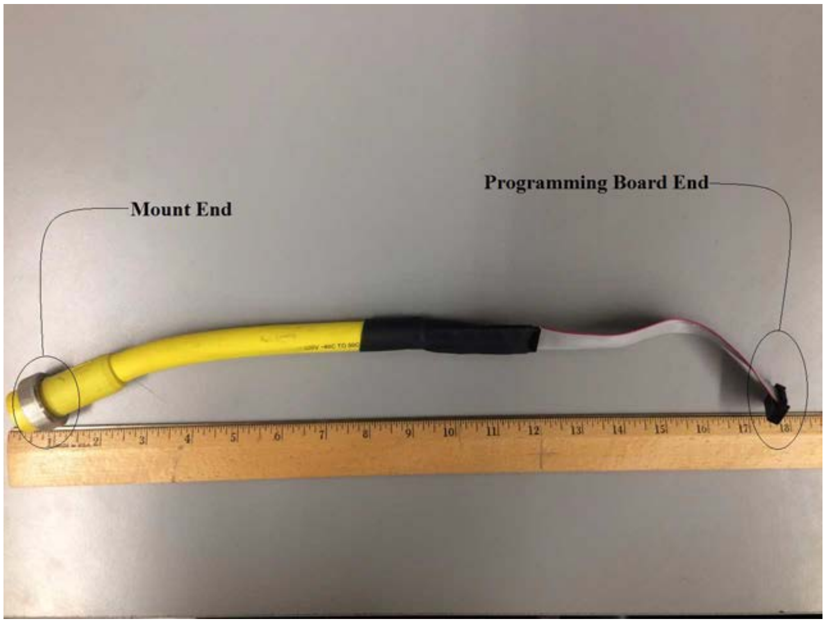

Figure 27. 3-Meter Programming Cable for Underwater MEMs Sensors

A cable that connects to the 12-pin mini-link at the back of the sensor housing was also designed to allow for a 5-volt bias input and sensor voltage output through 2 BNC connectors.

B. ASSEMBLING THE SENSOR IN PSF-2CST SILICON FLUID FOR PROGRAMMING AND TESTING

An air bubble introduced into the rubber housing containing the silicon oil can cause numerous detrimental factors to the sensor. First, the existence of an air bubble in the housing would cause a reflection of the incident sound wave to occur due to the large impedance mismatch between the air and silicone fluid. Secondly, an air bubble in the housing would move around the housing as the entire mount and housing changes orientation. If a jolt or vibration occurs to the assembly the air bubble has a chance to pass through where the sensor is. The rapid change in densities passing through the sensor wing could cause the sensor to break at its weakest point, in this case the pivot point or hinge point. To prevent air from entering the rubber housing, it was decided to assemble the mount with the sensor attached to the rubber housing and screwed tight with the O-ring, all submerged in a PSF-2cST silicone fluid bath. In theory, if the sensor was assembled entirely in the silicone fluid, no bubbles could be introduced to the system and inside the housing. A picture of the full sensor system after assembly is shown in Figure 28.

Figure 28. Fully Assembled Sensor

Once the sensor was in the housing with the PSF-2cST silicone fluid it was balanced and reprogrammed again using the cable in Figure 27. The balancing allows for a test for continuity between cables and connections prior to testing, as well as ensuring the right reference capacitance is applied for underwater testing. The added capacitance is high due to the offset in comb fingers discussed in Chapter IV. The reference settings of the MS3110 are shown in Appendices E–H for testing in air and water. Once programmed the sensors are ready to be characterized in the water.

C. SIMULATIONS OF SENSORS IN WATER

The frequency response simulations for the 5- and 10-micron sensor are shown in Figure 29. The same configuration was used in these simulations, except the medium was replaced with PSF-2cST silicone fluid.

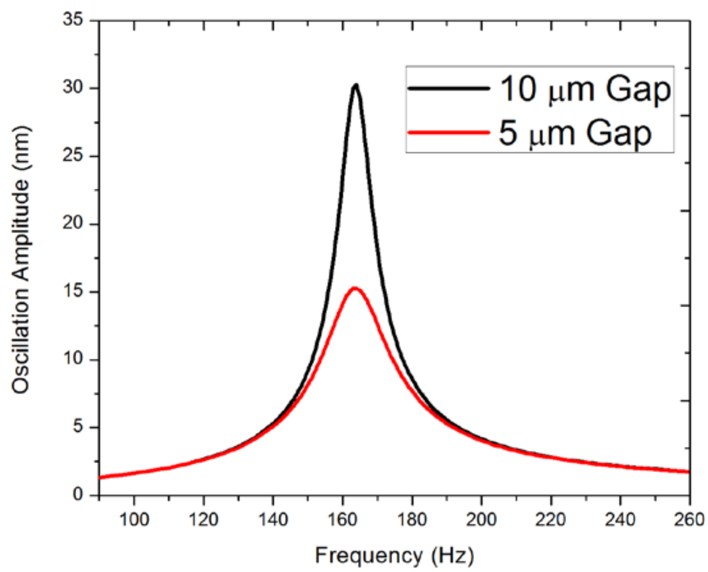

Figure 29. COMSOL Simulation of 5- and 10-Micron MEMs Underwater Sensor with Normal Incident Wave, Frequency Sweep 80–260 Hz

The simulation results, have the similar response as the sensor did in air for a frequency sweep showing a strong "bending" mode resonance peak. The major difference in these graphs and the air simulations of the sensors is the reduction in resonant frequency and the reduction in oscillation amplitude. The reduction in frequency and amplitude is due to the viscous solution and the drag caused on the wings operating in it as well as the mass loading by the oil. The damping changes the restoring force of the wing and causing the oscillation speed to be reduced. It is interesting to note that the 5- and 10-micron sensors have the same resonant peak frequency at 164 Hz based on the simulation, meaning the viscous oil has a greater effect than the mass difference due to the combs on the sensors. The sensors have different Q values but the same resonance frequency. The oscillation amplitude of the 10-micron sensor is twice the amplitude of the 5-micron sensor. The rotation of the incident angle of the plane wave at 164 Hz was simulated in COMSOL on each of the sensors. The results turned out to be the same as in air, each graph (see Figure 30) showing a cosine dependence on incident angle. The only difference between each sensor was the maximum oscillation amplitude.

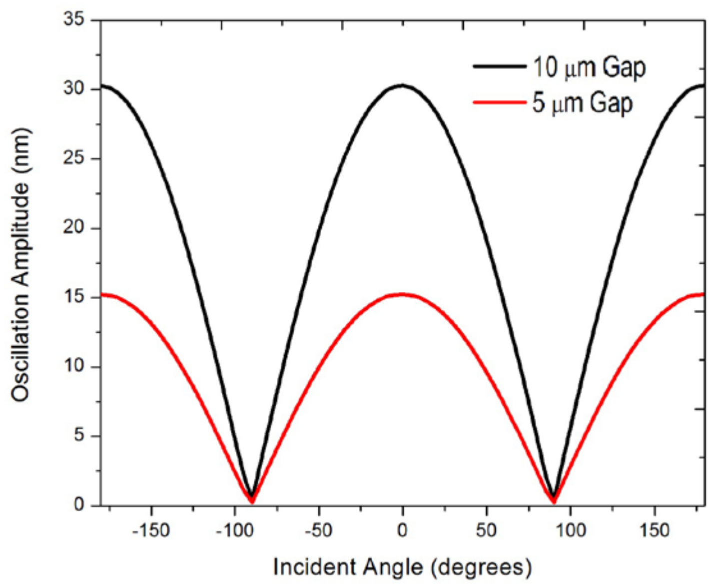

Figure 30. COMSOL Simulation 10-Micron and 5-Micron MEMs Sensor Changing Incident Angle of the Sound Wave Operating at 164 Hz

D. TESTING FACILITY FOR UNDERWATER TESTING

Naval Undersea Warfare Center (NUWC) in Rhode Island calibrates and characterizes sonar systems for the Navy and fortunately provided the ability to characterize the sensors in their facility. The specific vessel used for the measurement attempts is the System L test vessel or the “L-Tube” [12]. A picture of inside the L-Tube and the sensor mounted is shown in Figure 31.

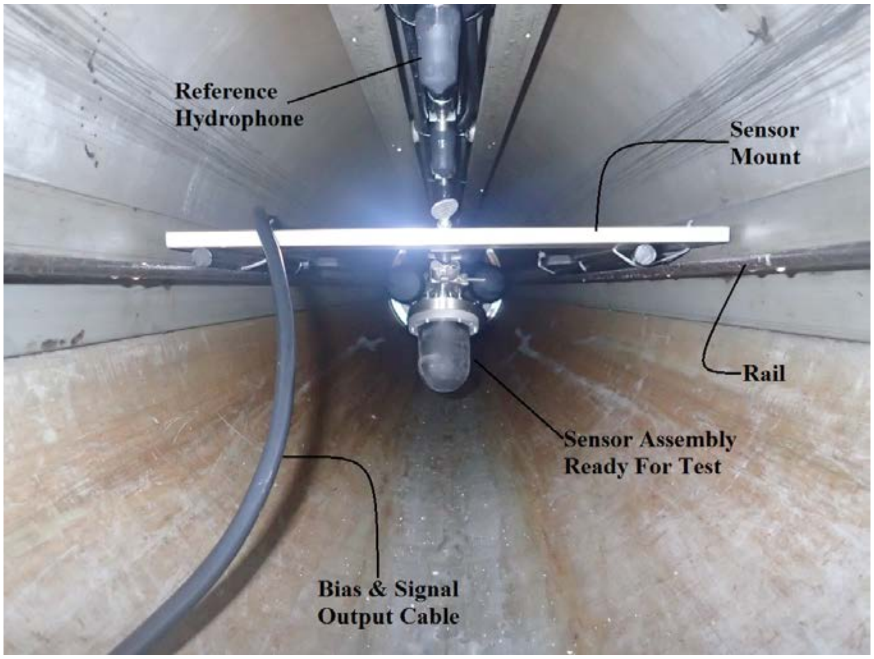

Figure 31. Inside System L Test Vessel with Generation 1 Sensor Assembly Mounted

The vessel is horizontally mounted, 243 cm in length, and has a diameter of 38 cm [12]. There are six reference hydrophones inside the tube that determine the exact pressure and characteristics of the sound wave as it travels through the tube. There are two sources at each end of the tube. Once the sensor is mounted in the tube and cables are routed through the tubes packing gland, a traveling wave is generated in the tube from a source located at one end of the tube. The other end has a source that is driven to eliminate reflections [12]. A picture of one of these sources is shown in Figure 32. This allows the simulation of a travelling plane wave.

Figure 32. Sound Source Located at Each End of System L Test Vessel

The sensor is placed next to a reference hydrophone which allows the sensitivity of the sensor to be determined. The tank was designed to operate at a frequency range of 1 Hz to 1.5 kHz [12].

E. TESTING AND ASSEMBLY

The sensor and equipment to assemble were all shipped by plane to Newport, Rhode Island in preparation for testing to be done at NUWC. In all, 5 separate sensors were brought. Two 5-micron sensors and three 10-micron sensors, three rubber housings, 4 stainless steel mounts with wiring, soldering and epoxy completed and tested satisfactorily were all brought to Rhode Island for assembly. The first day, three sensors were to be assembled, two 10-micron sensors and one 5-micron sensor, and brought to NUWC for testing. The two 10-micron sensor assemblies were programmed satisfactorily after being fully put together and showed they were ready for testing, but the 5-micron sensor assembly was not able to be programmed after assembly. It was disassembled, and it showed that the wing had broken off. It was assumed that air was accidently introduced or the sensor suffered too many vibrations during assembly. The other two sensors were brought to NUWC for testing. One of the 10-micron sensor was mounted incorrectly at first in the L-Test Vessel, and then when pulled from the vessel no longer showed programming capabilities. It was disassembled, and it was found that the wing had broken off at the pivot point. This was most likely due to an air bubble introduced in the rubber housing and the vibrations suffered during mounting the assembly in the L-Test vessel. The other 10-micron assembly was mounted in the vessel but when the first frequency sweep test was run the sensor showed no output. The sensor was taken out of the vessel and disassembled. The entire sensor wing and substrate had disconnected from the wire bonding. It is believed that the vibrations from shutting the L-Test vessel door prior to filling caused the sensor to disconnect. An image of this is shown below in Figure 33.

Figure 33. Destroyed Sensor after Being Pulled from L-Tube Test Vessel

The remaining two sensors were assembled with a new method of maintaining the sensor entirely submerged under the silicone fluid, even during the tightening of all the screws in the stainless-steel ring to the mount. Holes were poked into the epoxy that protected the soldering in the mount, because it was believed that air was introduced by escaping from the liquid tape once the oil was in the housing. The last 5-micron sensor assembly was not able to be programmed after assembly, and it was disassembled and shown the wing had broken at the pivot point. The 10-micron sensor assembly showed it could be programmed after assembly and was taken to NUWC for testing. The sensor assembly once brought to NUWC was checked again and did not respond. The sensor was disassembled, and it was discovered that the sensor wing had again broken at the pivot point. It is believed that an air bubble was introduced to the 5-micron assembly while attempting the new method of assembly. It is likely that the 10-micron assembly must have broken due to excessive vibrations.

F. LESSONS LEARNED FROM NUWC VISIT

The Gen 1 5- and 10-micron sensors are very sensitive to vibrations and impulse shocks. Four out of the five sensors brought to be tested at NUWC broke at the pivot point connecting the sensor wing to the substrate. A picture of this is shown in Figure 34.

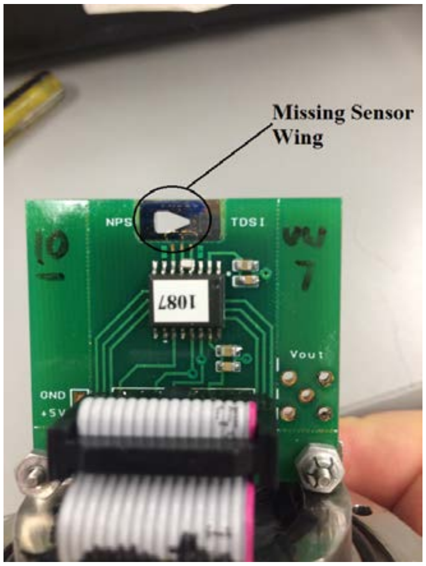

Figure 34. Generation 1 Underwater MEMs Sensors Broken at Pivot Point

Prior to traveling with the sensor wings to NUWC, a shock test was performed on a sensor submerged in silicone oil. Various stresses were placed on the sensor, but when the entire sensor was submerged in oil, it maintained its integrity and did not break at the pivot point. The only action shown to break the sensor wing was heavy consecutive hits to the sensor mount. Two Generation 2 sensors will be discussed in Chapter IV that could potentially solve the problem of the vulnerable sensor wing breaking at the pivot point by shortening the wing length. The Generation 1 sensor still needed to be tested in water to determine its capabilities. It is still believed that if all the air bubbles can be eliminated from the oil in the rubber housing, that the sensor will be able to maintain its integrity even if heavy vibrations occur. Two issues that were identified as possible causes of air entering the housing were the silicone oil not being degassed prior to use and that there was a lot more air coming from the epoxy region of the sensor mount than originally expected. These are two issues that will need to be examined by future tests and designs.

G. NPS TANK CHARACTERIZATION

The Naval Postgraduate School (NPS) tank is small and not anechoic in nature under 10 kHz, but it still can prove a good baseline for testing the Gen 1 sensors.

a. Frequency Sweep

The test performed on the sensor was a frequency sweep test, similar to what was performed in the air. An EV Commercial UW30 underwater loud speaker was mounted in the underwater NPS tank facility and connected to the SR865 lock-in amplifier for control. A Bruel & Kjaer Type 8103 reference hydrophone that was connected to a SR 560 low-noise preamplifier was placed at the exact location of the sensor to get a measurement of the source and the background. The set-up can be seen in Figure 35.

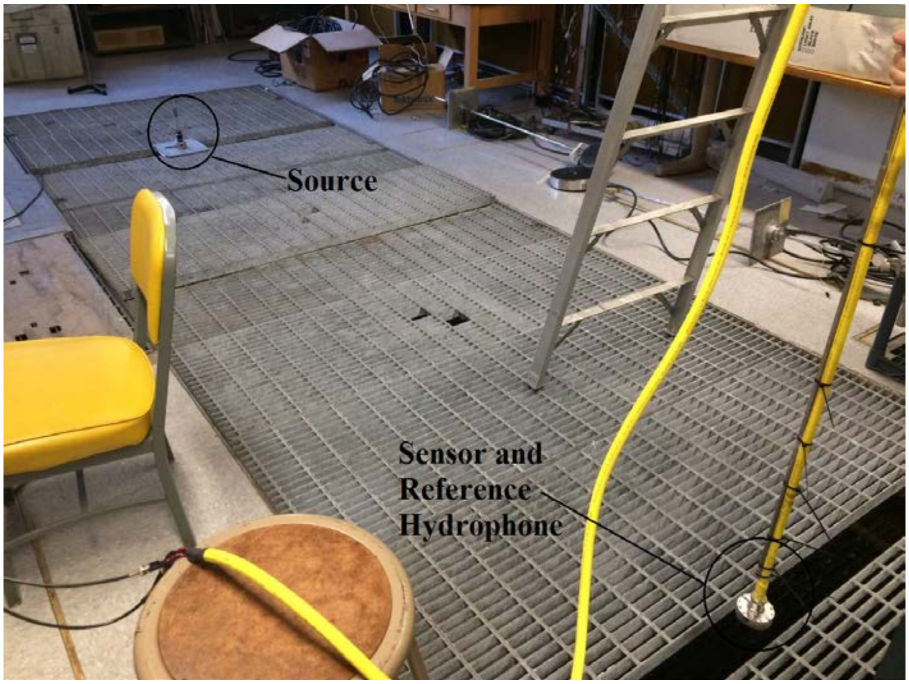

Figure 35. NPS Tank Facility Setup for Underwater Testing

A frequency sweep of the source recorded by the reference hydrophone is shown in Figure 36. The sensitivity of the hydrophone [13] and the pre-amp settings (Appendix I) were used to calculate the sound pressure.

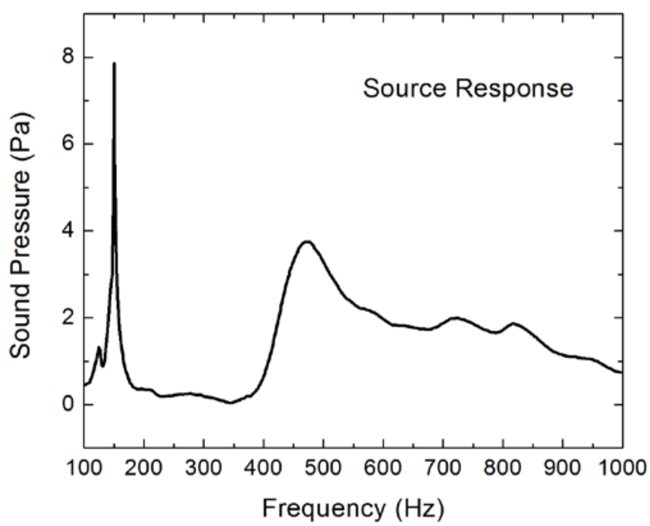

Figure 36. Reference Hydrophone Response to Frequency Sweep Test

It can be observed that the source exhibits a resonance around 140 Hz, which is very close to the simulated resonance of the sensor around 160 Hz. This can cause the response in this region of the spectrum to be unpredictable. In order to reduce the source effect of the measurements, for all acoustic intensities the sensor response was divided by the source response, in Pascals, providing the voltage output per pascal at all frequencies. A frequency sweep test on the 10-micron sensor at varying source levels is shown in Figure 37.

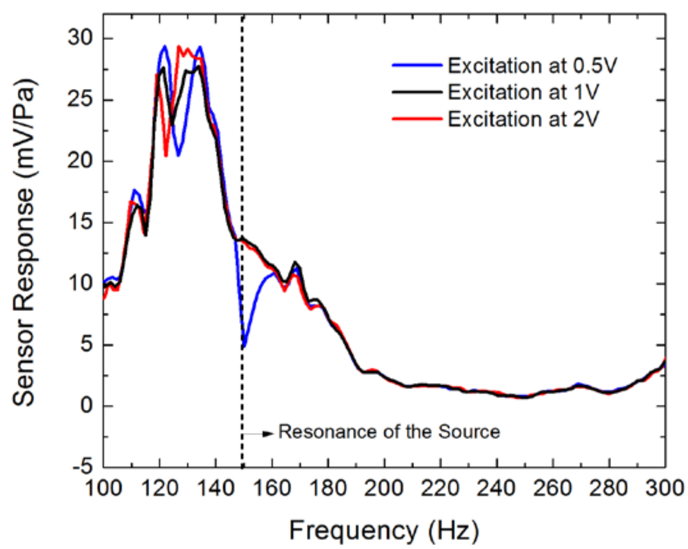

Figure 37. Gen 1, 10-Micron Underwater Frequency Sweep Results

Based on Figure 37, the 10-micron sensor is fairly consistent sensitivity when speaker output voltage is being changed. A set of peaks and valleys superimposed in the spectrum is most likely due to the resonant peak of the source interfering with the sensor response.

H. NPS CHARACTERIZATION TAKEAWAYS

The NPS testing facility creates some issues with testing the Gen 1 sensors. The tank is only anechoic above 10 kHz, which means there are multiple reflections created from the walls. Even so the sensor still showed consistent results when source power was adjusted. The sensor showed a sensitivity level in the range of mV/Pa, which is a much greater response than many standard hydrophones (μV/Pa). The initial tests using the NPS tank indicate that Gen 1 sensors are ready for further measurements in a tank that is better suited for low frequency testing of hydrophones.

THIS PAGE INTENTIONALLY LEFT BLANK

IV. CURVATURE OF THE SENSOR WINGS DUE TO RESIDUAL STRESS

The scanning laser vibrometer used in frequency sweep testing has the unique ability to make 3D images the surface of micro systems to create videos, as well as to determine all directions of motion and forces. In a 3D image of the 10-micron sensor taken by the scanning laser vibrometer, it was noticed that the capacitive comb fingers of the sensor were completely above the substrate fingers. This can be seen in the scanning electron microscope image shown in Figure 38.

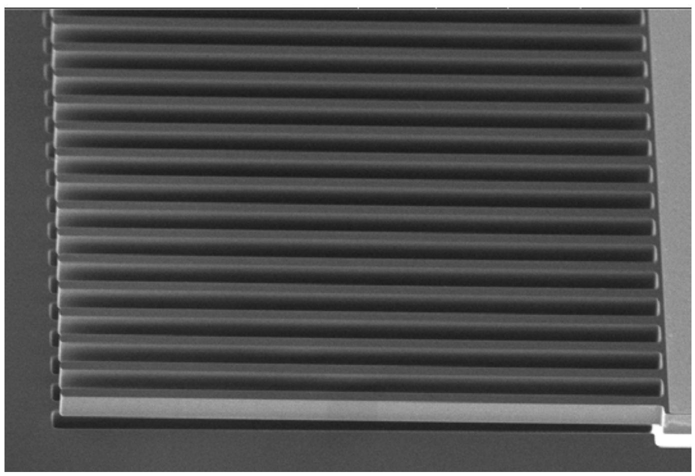

Figure 38. Image of 10-Micron Sensor at Rest Taken by Scanning Electron Microscope

The image shows that the sensor wing is completely lifted out of the substrate, near the end of the wing where the combs are. From this picture, two questions arise and need to be answered. To what extent are the comb fingers not overlapping with substrate fingers? How does this effect the sensitivity of the sensors?

A. RESIDUAL STRESS–GENERATED CURVATURE OF WING

1. Estimate of Curvature on Wing

The offset of the capacitive comb fingers on the MEMS sound sensors was first studied by Downey in his thesis work [14]. The cause for the curvature and residual stress on the wing occurs in the high-temperature doping step of the SOIMUMPS process, along with the trenching step mentioned in Chapter II [14]. The only distinguishing difference between the 10- and 5-micron sensors is the horizontal gap width between fingers which should not affect the amount of offset. The impact of the curvature on sensitivity will be investigated on both sensors. The entire curvature of the wing can be determined using a simple estimate formulated by Downey, if the following two assumptions can be made about the sensor [14]. First it is assumed that the doping layer thickness on the wing and the residual stress do not vary between different SOIMUMPs runs [14]. Secondly, it is assumed that the doping layer has a much smaller thickness than the total device layer thickness [14]. These assumptions can be made for the Generation 1 5- and 10-micron sensors employed in this work. It should also be noted that Downey's work was only on early generation MEMS sensor with a square wing shape. This will cause a slight variation, but the equation used is dependent on the thickness of the sensor wing and is expected to provide a good estimate of radius of curvature. The equation used for the estimation of radius of curvature (R) is given by [14]

$$R \approx \frac{{t_0}^2}{1.4}, \quad (4.1)$$

Where t_0 is the thickness of the device layer in microns [14]. The results of this calculation using a 25-micron thickness (the designed thickness of the sensor) is $R \approx 450\ mm$. The deflection of the wing using the estimated radius of curvature is shown in Figure 39.

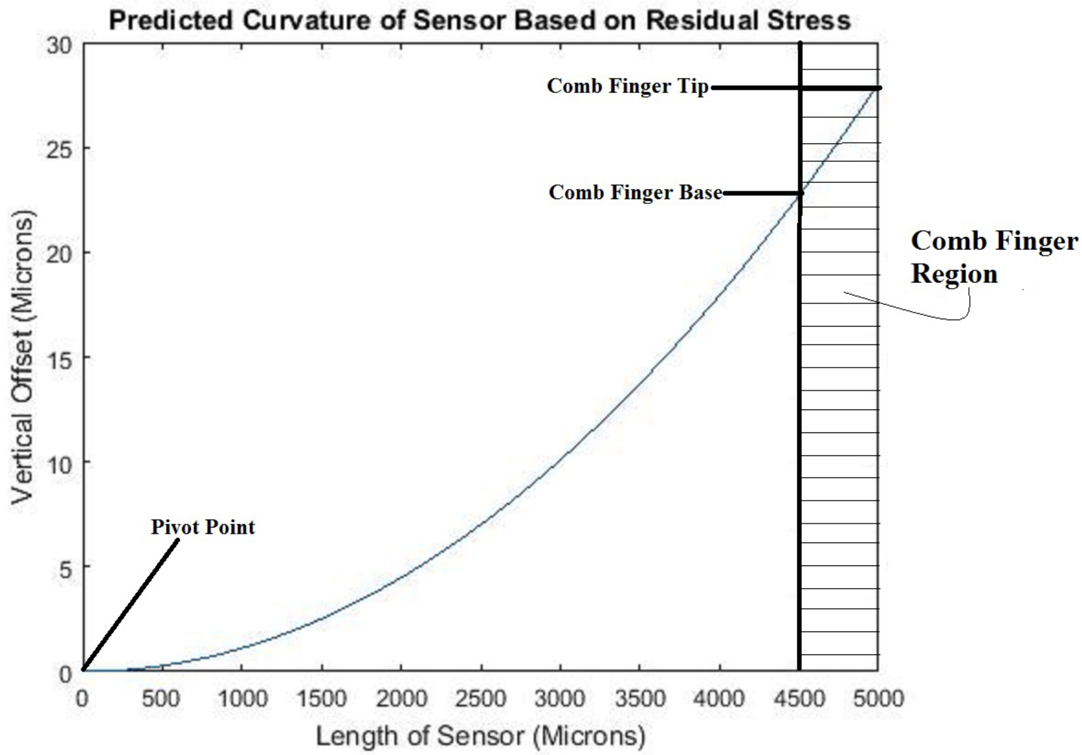

Figure 39. Graph Showing Projected Vertical Offset of the Sensor Wing Using Equation 4.1

This graph projects a total offset of about 28 microns at the tip of the wing where the combs are offset by at most 4 microns above the substrate.

2. Scanning Electron Microscope Images of Sensor

To measure the extent of the actual offset between the wing and substrate, the sensor was examined under a FEI Inspect 50 Scanning Electron Microscope (SEM). Using the SEM images in Figures 40 and 41 we were able to quantify the offset between the sensor and the substrate.

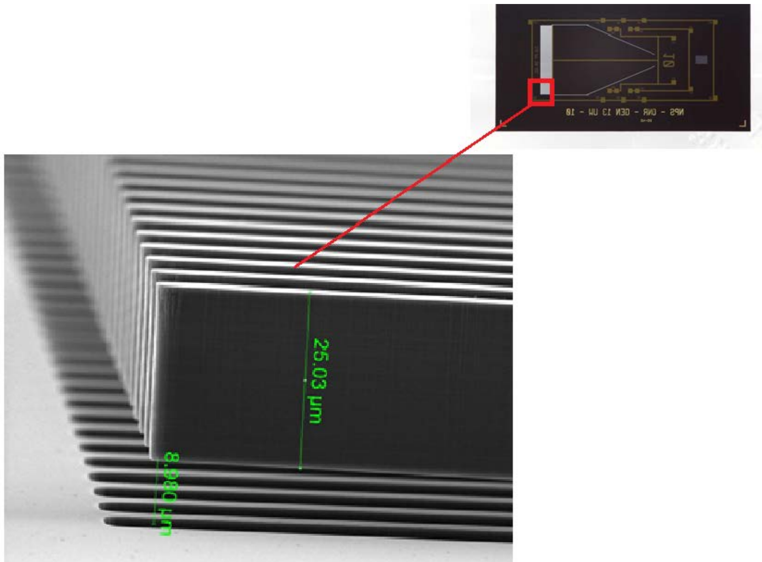

Figure 40. SEM Image of the Offset of the Sensor at the End of the Wing

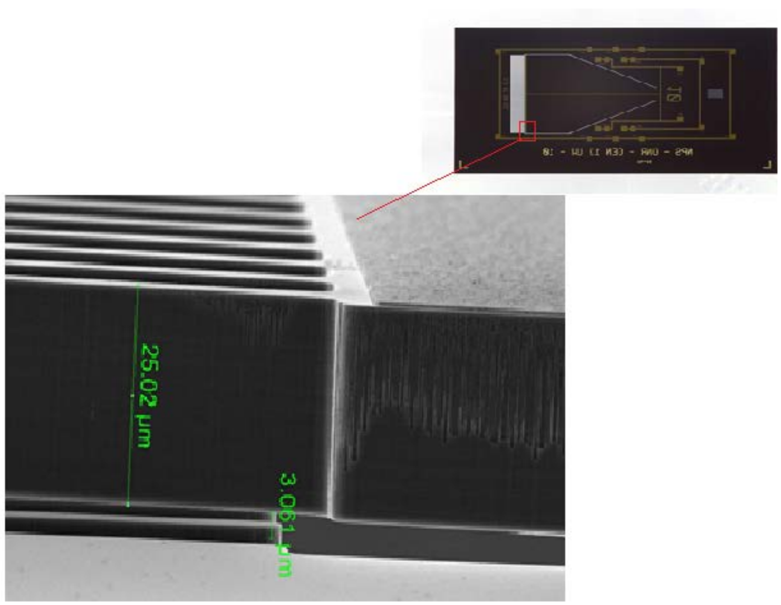

Figure 41. SEM Image of the Sensor at the Base of the Comb of the Fingers

The SEM images show that the sensor has an offset range of approximately 3 microns at the base of the comb fingers (Figure 41) and 9 microns at the end of the comb fingers (Figure 40), therefore, there is no overlap between the sensor combs and the substrate combs. The values of offset in Figure 40 and 41 are nearly twice the projected values of the prediction made in Figure 39. The lack of overlap could cause a reduction in the electronic sensitivity of the sensor.

B. ELECTRICAL SENSITIVITY EFFECTS BASED ON SENSOR OFFSET

Downey discovered that the overall electrical sensitivity decreases with a decrease in the capacitance of the sensor due to the offset [14]. The capacitance per unit length is given by [14]:

$$c(z) = \frac{\varepsilon_0 * (t-z)}{d} \quad , \tag{4.2}$$

where ε_0 =8.85x10^{-12} F/m is the permittivity of free space, t is the thickness of the sensor wings, z is the amount that the wing comb fingers tips are raised above the position (in this case roughly 34 microns based on Figure 40 and d is the gap between combs (5 or 10 microns). This formula is highly accurate when z < t which is not true in our case but will be shown for comparison [14]. The second equation, known as the two-plate model, is given by [14]

$$c(z) = \frac{\varepsilon_0 * w}{z-t} \quad , \tag{4.3}$$

where w is width of the comb fingers (10 microns). This equation was shown by Downey to be highly accurate when z >> t. A comparison of effect of offset on capacitance using equations 4.2 and 4.3 should show how the curvature affects the electrical output of the sensors. The region where z > t but not z >> t can be interpolated using the graph of each equation. Equations 4.2 and 4.3 for the 5 and10-micron sensor are plotted in Figure 42.

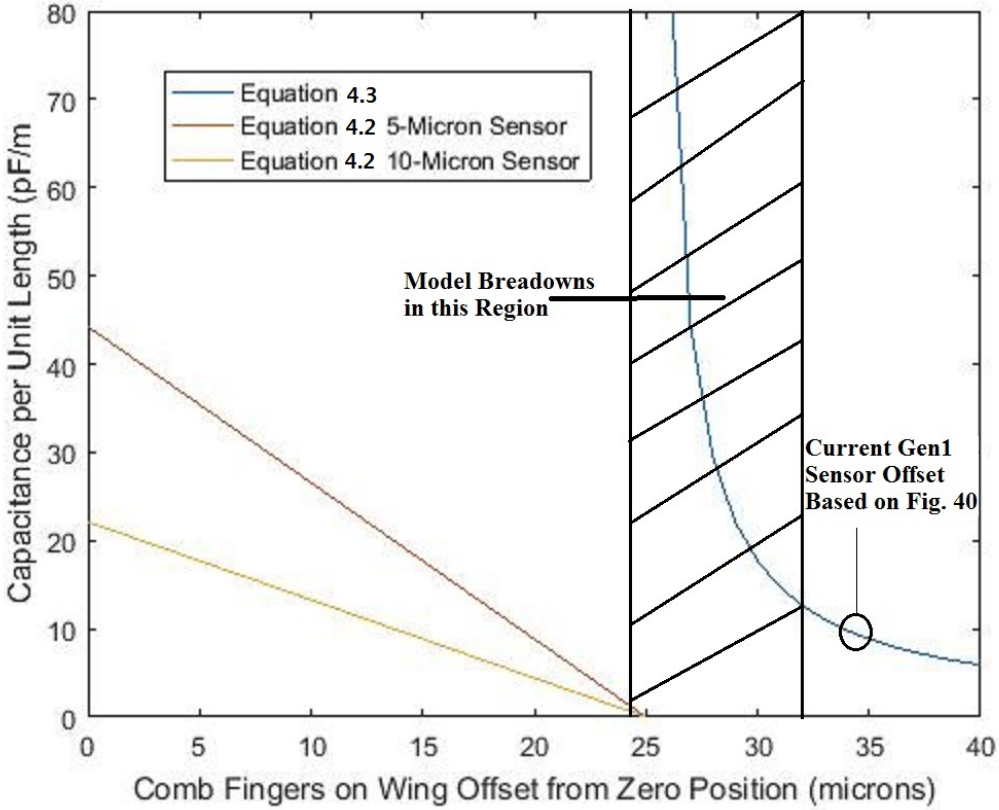

The graph shows the results of equation 4.2 for both the 5 and 10-micron sensor and the results from equation 4.3 which has no reliance on gap width, "d". There is a region where the model breaks down because it does not fit the criteria of the two equations. The current position of the Gen 1 sensor and its offset is indicated.

Figure 42. Comb Fingers on Wings Offset versus Capacitance per Unit Length Graph

Equation 4.2 estimates capacitance while there is "some" overlap between the comb fingers on the wing and the fingers on the substrate (0 to 25 microns on graph) whereas Equation 4.3 estimates capacitance when the offset of the wing is much greater than the 25 microns. This leads to the area in Figure 42 where the model breaks down. The equations are approximations, and there are some capacitive effects not considered in both equations such as "fringing effects" [14]. It is easy to see that the capacitance could be improved dramatically on our current sensor if it moved into the region governed by equation 4.2 where capacitance increases linearly as offset decreases. This initial capacitance is important, because the electronic sensitivity of the sensor increases linearly with the bias capacitance [14]. The greater the initial capacitance is the greater the change in capacitance is when the wing oscillates. To optimize electronic sensitivity, it is necessary to have higher overlap between the combs.

C. RESIDUAL STRESS–GENERATED CURVATURE OF WING CONCLUSION

The Gen 1 sensors were successfully characterized in air and showed promising results underwater. The sensor was also shown not to be fully optimized due to a residual stress induced offset placed on the sensor wing from the fabrication process. This offset leads to a decrease in initial capacitance which could result in an overall reduction in electrical sensitivity.

THIS PAGE INTENTIONALLY LEFT BLANK

V. GENERATION 2 UNDERWATER MEMS SENSORS

As Downey's equation predicted and was confirmed in the SEM images shown in Figures 40 and 41, there is an offset in the comb fingers due to the residual stress introduced by fabrication. This affects the capacitance of the sensor at rest and therefore the readout sensitivity. We explored Downey's equation which slightly underestimated the actual maximum offset seen in the Gen 1 sensors by about 17%. By looking at the graph in Figure 39, if thickness (t_0) remains constant, to reduce the offset the wing length needs to be shortened. These results led to the design of MEMS Generation 2 underwater sensor modifications 1 and 2, or simply referred to as "Gen 2 Mod 1" and Gen 2 Mod 2". Figures 43 and 44 show the basic 2D drawing of the sensors. The COMSOL settings used to design the Gen 1 underwater sensors were used to design the Gen 2 sensors. The goals were to simply make the wing length shorter to combat the comb fingers offset caused by residual stress, make the wing sturdier by decreasing the wing length to pivot ratio and to explore the changes in resonance frequency by adjusting the pivot points to different dimensions. The sensors both have a 10 micron gap width and maintain 25 microns thickness. The shorter wing length and thicker pivot should make the sensors stronger and less susceptible to damaging and breaking like the Gen 1 sensors encountered.

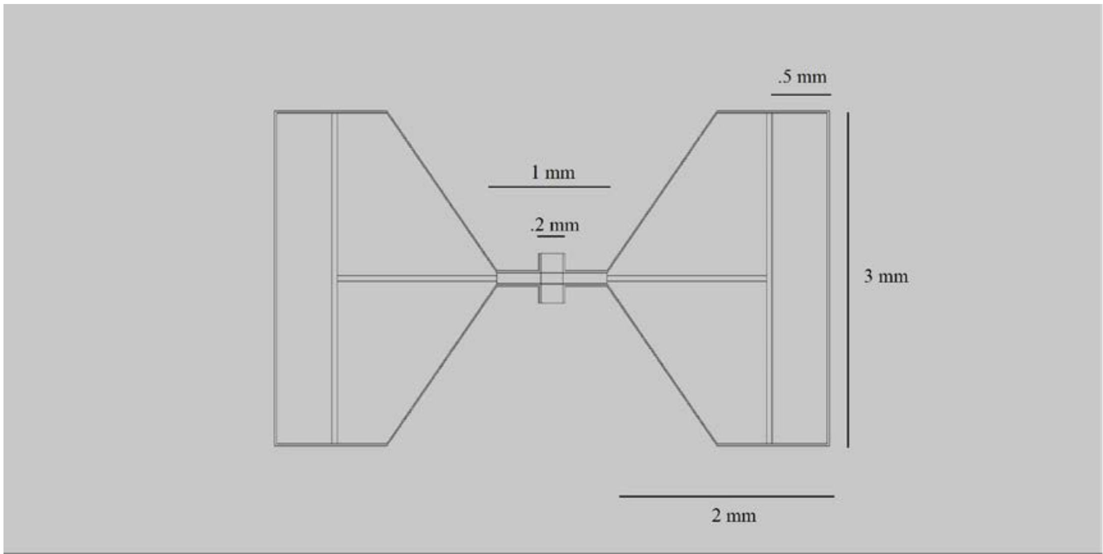

Figure 43. MEMS Underwater Sensor Generation 2 Modification 1, Referred to as “Gen 2 Mod1” 2-Dimensional COMSOL Drawing

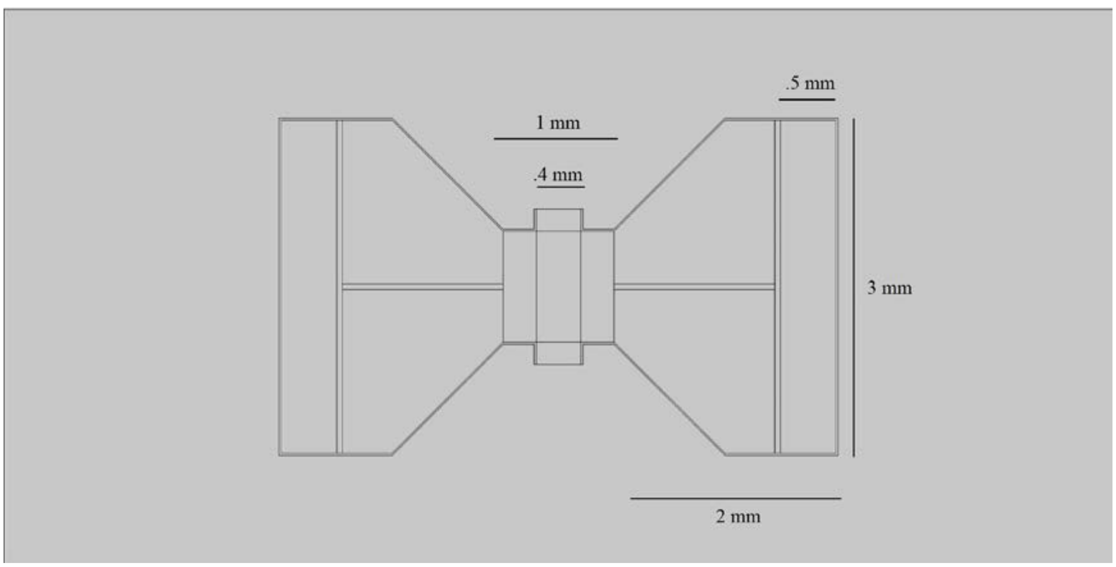

Figure 44. MEMS Underwater Sensor Generation 2 Modification 2, Referred to as “Gen 2 Mod 2” 2-Dimensional COMSOL Drawing

There are some major differences in the Gen 2 sensors to that of the Gen 1 sensors. First and foremost, the wing length is reduced from 5000 microns to 2500 microns for both Gen 2 Mod 1 and 2. This shortening in wing length will cause the pre-existing offset to be reduced significantly. Using Figure 42 and equation 4.1, a 2500 micron wing length, while maintaining the thickness at 25 microns, results in an offset at the tip of the comb fingers of only 5 microns. Even if equation 4.1 underestimates the offset slightly, this would be a marked improvement in overall offset and will also result in a capacitance per unit length of close to double that of the Gen 1 10-micron sensor. To verify the offset of the Gen 2 sensors, both were inspected using the SEM and the images are shown in Figure 45 and 46. Both the Gen 2 Mod 1 and 2 have the same wing length and design, and it resulted in relatively the same offset between the two after inspected in the SEM.

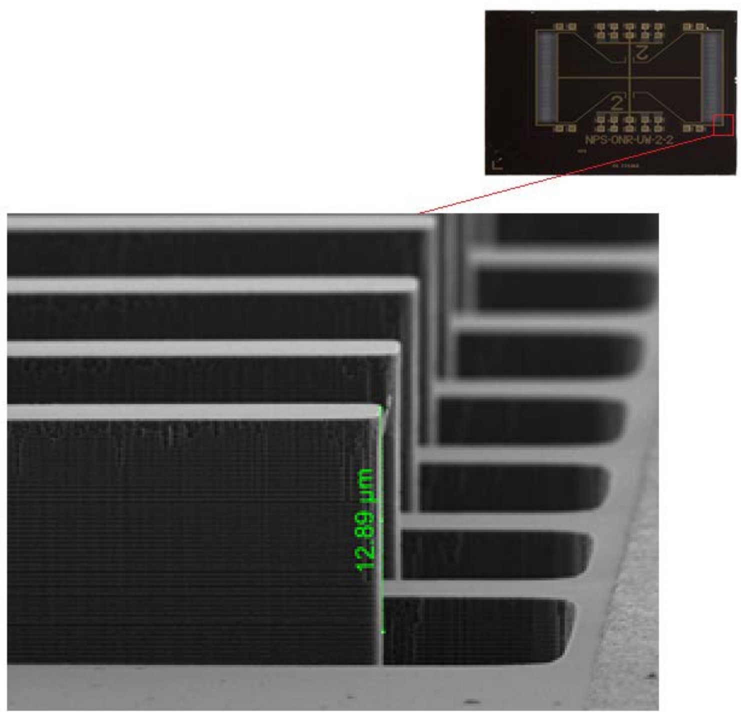

Figure 45. SEM Image of Gen 2 Sensor Offset Near End of Comb Fingers

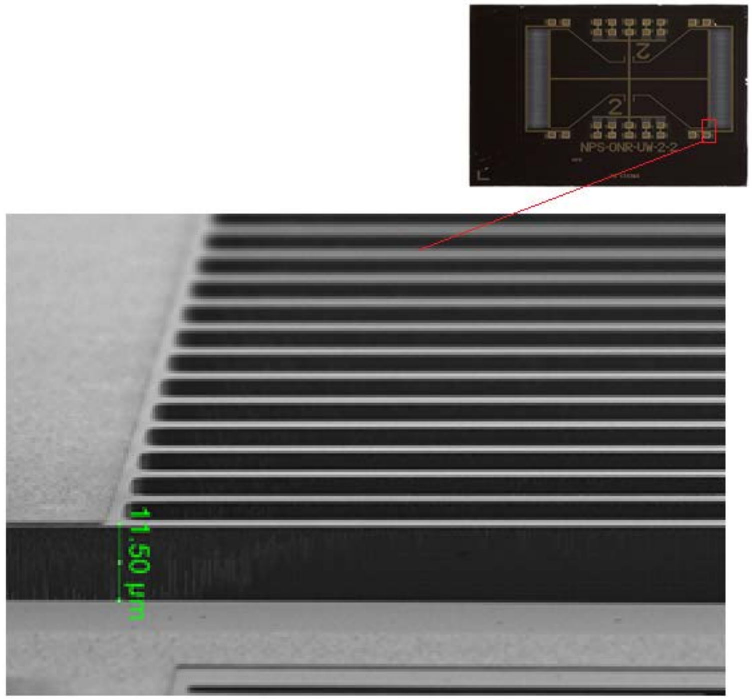

Figure 46. SEM Image of Gen 2 Sensor Offset Near End of Comb Fingers

The figures show that the offset between the comb fingers is roughly 13 microns at the end of the combs and 11.5 microns at the base of the combs. Although Downey's equation underestimated these offsets again, this is a drastic improvement in offset from the Gen 1 sensor design. This offset improves the initial capacitance per unit length by double what it was before in the Gen 1 sensor.

The other major difference between the Gen 1 and Gen 2 is the two-wing design vice the one wing design. The addition of a second wing allows for the utilization of the rocking mode shown in figure 2. The only difference between Gen 2 Mod 1 and Gen 2 Mod 2 is the hinge that is connected to the wing itself and allows for the wing to oscillate. The change in size of this hinge and how it connects to the wing will change the operating "bending" resonance frequency. A picture of the fabricated Gen 2 Mod 2 Sensor is shown in Figure 47.

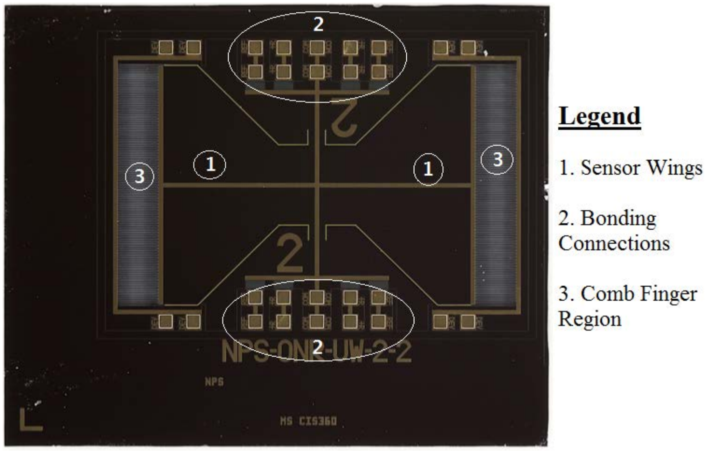

Figure 47. Generation 2 Modification 2 Fabricated Sensor

A. COMSOL SIMULATIONS IN AIR OF GEN 2 SENSORS

Each of the Gen 2 Mods were modeled in COMSOL, and the simulated frequency responses in air are shown in Figures 48 and 49. These sweeps are the same done on the 5- and 10-micron sensor to simulate the actual testing done in the anechoic chamber.

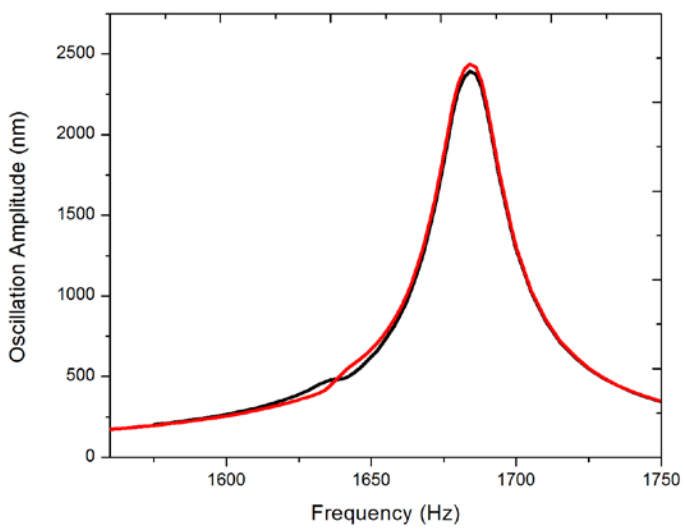

The graph shows the amplitude response of a normal incidence wave on the Gen 2 Mod 1 sensor. The red line represents one of the wings and the black line represents the other wing's amplitude response.

Figure 48. COMSOL Simulation Gen 2 Mod 1 MEMs Underwater Sensor, Normal Incident Wave, Frequency Sweep 1400–1800 Hz

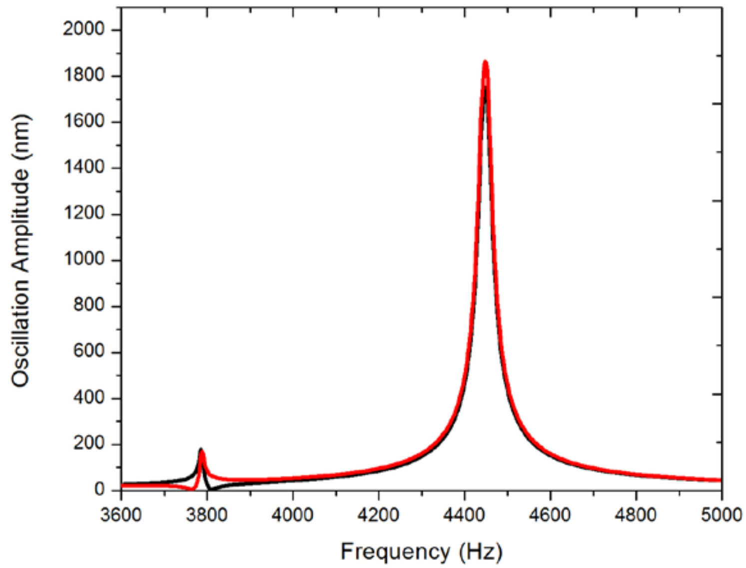

The graph shows the amplitude response of a normal incidence wave on the Gen 2 Mod 2 sensor. The red line represents one of the wings and the black line represents the other wing's amplitude response.

Figure 49. COMSOL Simulation Gen 2 Mod 2 MEMs Underwater Sensor, Normal Incident Wave, Frequency Sweep 3600–5000 Hz

The simulations show that the Gen 2 Mod 1 has a clear "bending" mode resonant peak at 1684 Hz while the Gen 2 Mod 2 "bending" mode resonant peak is at 4448 Hz. The peak at 3790 Hz is due to the rocking motion. The "bending" mode frequencies are much higher than the Gen 1 underwater sensors due to the smaller wing area.

B. CHARACTERIZATION OF GEN 2 SENSORS IN AIR

1. Anechoic Chamber Characterization

The sensors were assembled on the PCB and the MS3110 was programmed according to the values given in Appendix H and I. It is important to note that only one wing was bonded to the PCB due to limitations of the built-in reference capacitor, this can be easily fixed by using an external capacitor.

The Gen 2 sensors were characterized in air in the anechoic chamber. The source was mounted at the same distance the only difference between tests was the JL speaker was changed out for a JBL Model 2380A. The results of the frequency sweep performed on both the Gen 2 Mod 1 sensor and the Gen 2 Mod 2 sensor are shown in Figure 50 and 51.

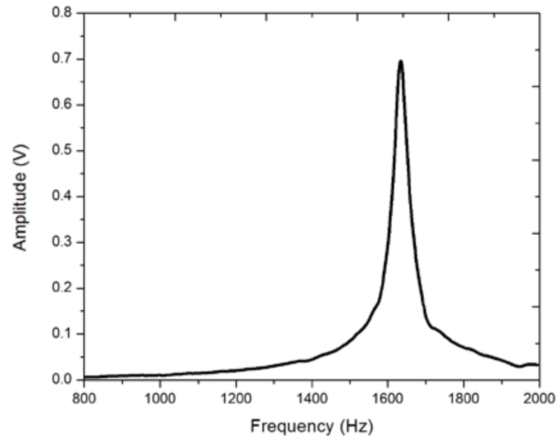

Figure 50. Gen 2 Mod 1 Sensor Frequency Sweep Test, Normal Incidence, 800-2000Hz, Sound Pressure at Sensor 334 mPa

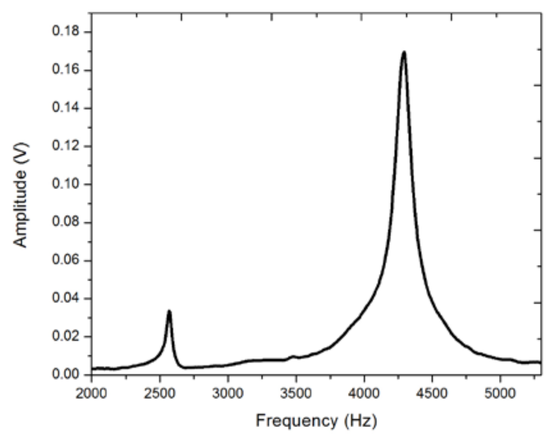

Figure 51. Gen 2 Mod 2 Sensor Frequency Sweep Test, Normal Incidence, 2000–5500Hz, Sound Pressure at Sensor 238 mPa

The Gen 2 sensors both showed results that were expected based on the COMSOL simulations. The Gen 2 Mod 1 sensor showed a “bending” mode frequency at 1634 Hz and the Gen 2 Mod 2 showed a “bending” mode frequency of 4291 Hz. The experimental resonance frequencies were lower than the simulated ones. This again is caused by the COMSOL simulation using design values for thickness which may be slightly less than actual values of the fabricated sensor.

2. Sensitivity

The sensitivity of the sensor was determined by performing a series of measurements using the G.R.A.S. Free Field Microphone Type 40 AF. The microphone was mounted at the same distance from the speaker as the sensors just as it was with the Gen 1 sensors described in Chapter II. Again the sensitivity, [V/Pa], is dependent on the gain of the MS3110, which depends on the programming parameters shown in Appendix H and I. They were kept almost the same for both Gen 2 sensors to provide a fair comparison. Two measurements for each sensor with different speaker output powers were taken to determine the sensitivity in air. The results of this sensitivity analysis are shown in Table 5 and 6. The reduction of sensitivity for Gen 2 Mod 2 is due to the lower amplitude of vibrations at high resonant frequencies as seen in Figure 48 and 49.

Table 5. Sensitivity Measurement of Gen 2 Mod 1 MEMs Underwater Sensor Tested in Air

Speaker Output (V_{rms})	Reference Microphone (mV)	Sound Pressure at Sensor (mPa)	Gen 2 Mod 1 MEMs Underwater Sensor output (mV)	Gen 2 Mod 1 MEMs Sensor Sensitivity at 1634 Hz (V/Pa)
0.25	7.54	166	354	2.13
0.5	15.02	334	699	2.09

Table 6. Sensitivity Measurement of Gen 2 Mod 1 MEMs Underwater Sensor Tested in Air

Speaker Output (V_{rms})	Reference Microphone (mV)	Sound Pressure at Sensor (mPa)	Gen 2 Mod 2 MEMs Underwater Sensor output (mV)	Gen 2 Mod 2 MEMs Sensor Sensitivity at 4291 Hz (V/Pa)
0.25	5.40	119	87	0.73
0.5	10.77	238	170	0.71

The sensitivity for both the sensors in air are shown to be 2.10 V/Pa for the Gen 2 Mod 1 sensor and .73 V/Pa for the Gen 2 Mod 2 sensor.

C. COMSOL SIMULATIONS OF GEN 2 MOD 2 SENSOR IN WATER

The Gen 2 Mod 2 sensor was simulated to determine its response in silicone oil with regards to its “bending” mode resonant frequency. The Gen 2 Mod 2 was chosen for simulation and testing because of its higher expected resonance peak, which would be more easily tested in the NPS tank test facility. In the new medium, a lower Q value and a lower resonant frequency is expected because of the damping effect and mass of the PSF-2cST silicone oil. The normal incidence frequency sweep on the Gen 2 Mod 2 is shown in Figure 52

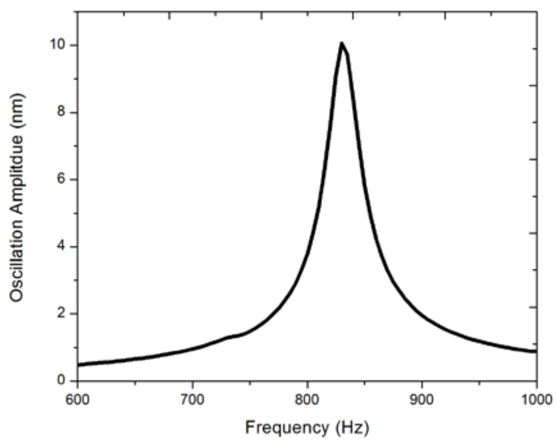

Figure 52. COMSOL Simulation Gen 2 Mod 2 MEMs Underwater Sensor, Normal Incident Wave, Frequency Sweep 600–1000 Hz

The “bending” mode resonant frequency for the Gen 2 Mod 2 is around 830 Hz. The biggest takeaway from the COMSOL underwater simulations on the Gen 2 Mod 2 sensor is the low amplitude of the oscillations of the sensor wings. The amplitude is much smaller than the simulations of the Gen 1 sensors at the same conditions. This will cause a smaller differential capacitance at resonance and a smaller voltage output. This is due to the smaller wing length of the Gen 2 sensors. The “bending” mode resonant frequency of the Gen 2 Mod 2 was much lower than in the air simulations, which was also expected due to the fluid loading.

D. UNDERWATER CHARACTERIZATION OF GEN 2 MOD 2 SENSOR

The Gen 2 Mod 2 sensor was characterized in the NPS tank facility in the same fashion as the 10-micron sensor. The sensor was mounted and assembled using the assembly shown in Chapter III. The acoustic source and background taken using the reference hydrophone was divided out of the sensor reading, and the response to numerous source output voltages were obtained. The set-up and distance from speaker to source was the same as in Figure 35. The frequency response in mV/Pa for 3 different excitation levels is shown in Figure 53.

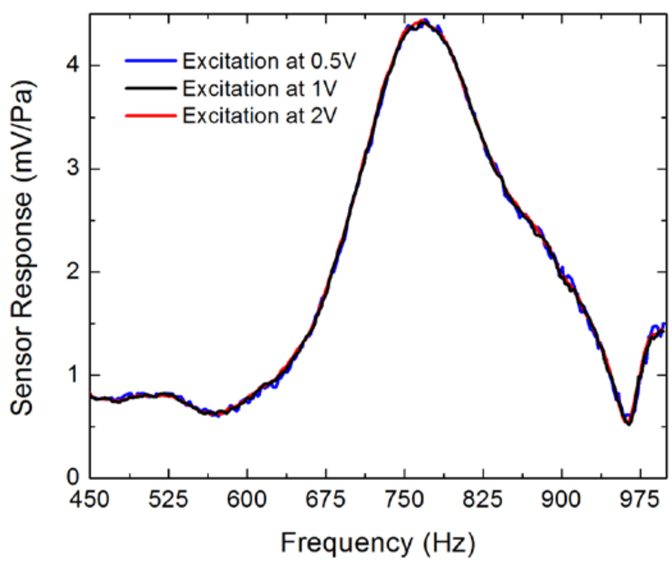

Figure 53. Underwater Frequency Response Results of Generation 2 Modification 2 Sensor

The curve exhibits a clear “bending” mode resonant peak at roughly 792 Hz which is very close to the predicted peak position in COMSOL. The Q is much lower than in the COMSOL simulation but that could be due to reflections and multiple arrival paths. This result indicates that the sensor exhibits a bending resonance mode underwater that could lead to sinusoidal directionality. The output is still in the mV/Pa which is quite high for an underwater hydrophone (typical hydrophones are operate in the $\mu V/Pa$ range). The Gen 2 Mod 2 needs to be further tested in a facility that can support testing that minimizes reflections.

THIS PAGE INTENTIONALLY LEFT BLANK

VI. CONCLUSIONS

A. SUMMARY OF RESULTS

Four *Ormia Ohracea* sensors have been designed and characterized both in air and underwater. Two Gen 1 single wing sensors have been designed in COMSOL and their frequency and directional responses were modeled. The two Gen 1 sensors with 10-micron and 5-micron comb gaps have shown high sensitivity (V/Pa) in air. They have also shown “bending” mode resonances in air and cosine dependence on direction of sound. The experimental results have led to refined drag equations that lead to better COMSOL simulations. The sensors were examined using a scanning electron microscope and found to have residual stress-induced curvature of the wings. This stress led to the comb fingers on the wing not overlapping with the combs on the substrate, which reduced the resultant capacitance. The sensors were also taken to NUWC in Rhode Island for underwater characterization but did not make it through testing due to vibrations damaging the sensors. The 10-micron gap sensor did show good response (mV/Pa) in an NPS tank facility that is not optimal for low frequency testing.

Two Generation 2 two-wing sensors were designed and fabricated to fix some of the problems that were found in the Generation 1 sensors. The Gen 2 has a stronger base, shorter wing length and showed good performance in the anechoic chamber giving expected frequency and directional responses. Both the sensors showed a 66% improvement in comb finger overlap which leads to a much-improved capacitance. The Gen 2 Mod 2 sensor was successfully tested in the NPS tank facility and has shown that a MEMS sensor can be used for as an effective narrowband threat detector in the undersea domain. Both the Gen 1 and Gen 2 sensors have shown sensitivities of mV/Pa in underwater testing which is a much higher sensitivity than most underwater hydrophones (μV/Pa). The Gen 2 sensors are ready for further testing and directional testing in a facility that will limit reflections.

The ability these sensors have shown could lead to a narrowband sensor that will drastically improve the directional capabilities of underwater sensors. The sensors, if further developed and improved, may lead to a sensor of miniscule size with directional capabilities and a much higher sensitivity.

B. RECOMMENDATIONS FOR FUTURE WORK

First and foremost, a tank or facility needs to be found to further refine the underwater frequency sweep tests performed on both the Gen 1 and Gen 2 sensors as well as assess the direction finding capability. Also, a low frequency sound source needs to be acquired to assess the low frequency response.

A full characterization of the Gen 2 Sensors in air needs to be conducted exploring rotational tests at ‘rocking” modes and quality factor assessments, and a direct comparison of the sensitivity between the Gen 1 and Gen 2 sensors should be made based on the length of the sensors and their responses.

APPENDIX A. TRANSMISSION AND IMPEDANCE CALCULATIONS FOR FLEXANE 80 RUBBER CASE

c = 2400 +/- 25 m/sec speed of sound in Flexane 80 [5], [15]

Specific Volume= 26.5 in^3 /lb, ρ = 1045 kg/m^3 Flexane 80 [5], [15]

$$r = \rho * c = 2.51*10^6 \, Pa*s/m \text{ for Flexane 80 [5]}$$

For case in air [5]:

$T = (\frac{2r_1}{k_2 L r_2})^2$ r=the specific acoustic impedance of the materials in this case the Flexane 80 and air, k = wave number

$r_1 = 415$ Pa * s / m. for air

At the frequency band used for air testing for this sensor, $k_2L = 0.005$.

T = $3.4*10^{-3}$ [5]

For case in water [5]:

Based on the layer of Flexane 80 being thin compared to wavelength in water and silicon oil

$$T = \frac{(4r_3r_1)}{(r_1+r_3)^2}$$

$r_1 = 1.48 \times 10^6$ Pa * s / m.[5] acoustic impedance fresh water

$r_3 = 9.41 \times 10^5$ Pa * s / m. [5] acoustic impedance silicon oil

T = 0.95 [4]

THIS PAGE INTENTIONALLY LEFT BLANK

APPENDIX B. LOCK-IN AND PREAMP SETTINGS (AIR TESTING SETUP)

A. 10-MICRON SENSOR SETUP

(1) SR865 Lock-in Amplifier Settings [16]

Sensitivity: 200 mV

Time Constant: 30 msec

Range: 300mV

Filter: 6dB slope

Sweep time: 100 sec

(2) HP467A Power Amplifier Output to Speaker

Lock-in output set to 1 V pk-pk with 10X gain from amplifier

B. 5-MICRON SENSOR SETUP

(1) SR865 Lock-in Amplifier Settings [16]

Sensitivity: 200 mV

Time Constant: 100 msec

Range: 300mV

Filter: 6dB slope

Sweep time: 100 sec

(2) HP467A Power Amplifier Output to Speaker

Lock-in output set to 1 V pk-pk with 10X gain from amplifier

C. GEN 2 MOD 1 SENSOR SETUP

(1) SR865 Lock-in Amplifier Settings [16]

Sensitivity: 100 mV

Time Constant: 10 msec

Range: 1V

Filter: 6dB slope

Sweep time: 100 sec

(2) HP467A Power Amplifier Output to Speaker

Lock-in output set to 1 V pk-pk with 10X gain from amplifier

D. GEN 2 MOD 2 SENSOR SETUP

(1) SR865 Lock-in Amplifier Settings [16]

Sensitivity: 100 mV

Time Constant: 10 msec

Range: 1V

Filter: 6dB slope

Sweep time: 100 sec

(2) HP467A Power Amplifier Output to Speaker

Lock-in output set to 1 V pk-pk with 10X gain from amplifier

APPENDIX C. UNDERWATER SIGNAL CABLE TO RIBBON CABLE SPLICE WIRING CHART FROM [5]

A. RIBBON CABLE

Pin #	Pin	Pin	Pin#
1 (red)	HV16	--	2
3	--	V2P25	4
5	+V	--	6
7	TESTSEL	--	8
9	V OUT	--	10
11	-V GND	CHPRST	12
13	--	SCLK	14
15	WRT	SDATA	16

B. UW CABLE

1	RED/BLACK
4	WHITE/BLACK
5	BLUE
7	ORANGE
9	RED
11	GREEN
12	GREEN/BLACK
14	BLACK/WHITE
15	ORANGE/BLACK
16	BLUE/BLACK

THIS PAGE INTENTIONALLY LEFT BLANK

APPENDIX D. PICTURES OF WIRE SOLDERING FOR SENSOR CASING AND ADAPTATION

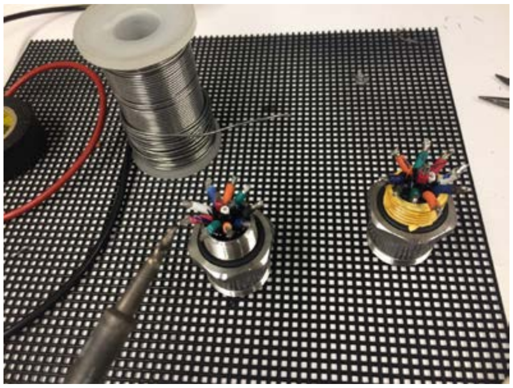

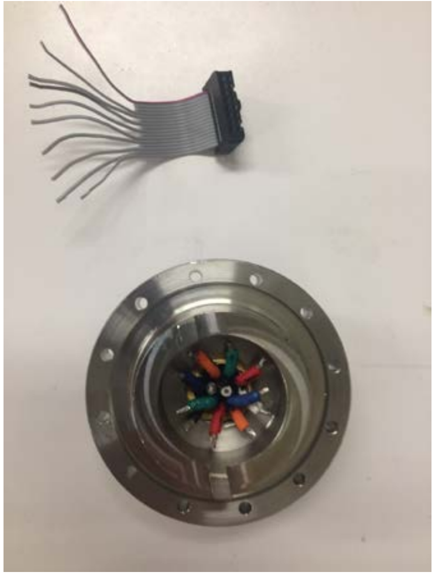

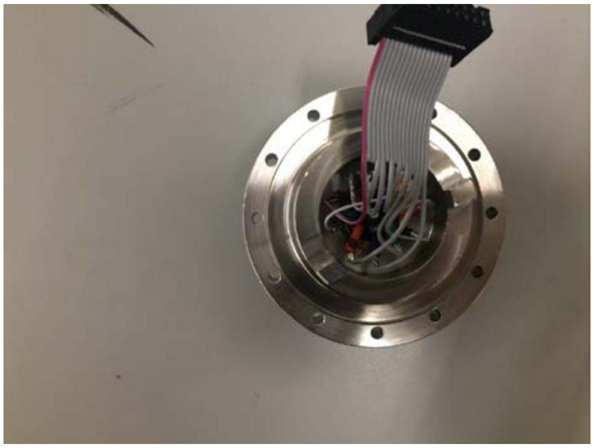

THIS PAGE INTENTIONALLY LEFT BLANK

APPENDIX E. MS3110 SETTINGS FOR 5-MICRON UNDERWATER SENSOR (AIR APPLICATION)

Current Reference Trim	Nominal
Voltage Reference Trim	Nominal
Oscillator Trim	Nominal
Output Buffer Gain Trim	Nominal
Output Buffer Offset Trim	Nominal
Output Buffer Output Offset Level Control	2.25V
Continuous-Time LPF Bandwidth Trim	3.0 KHz
Output Buffer Gain Select	2
IAMP Feedback Capacitor Selection	1.007 pF
IAMP Balance Capacitor Trim	7.619 pF
IAMP Balance Trim Capacitor Selection	0.171 pF

THIS PAGE INTENTIONALLY LEFT BLANK

APPENDIX F. MS3110 SETTINGS FOR 10-MICRON UNDERWATER SENSOR (AIR APPLICATION)

Current Reference Trim	Nominal
Voltage Reference Trim	Nominal
Oscillator Trim	Nominal
Output Buffer Gain Trim	Nominal
Output Buffer Offset Trim	Nominal
Output Buffer Output Offset Level Control	2.25V
Continuous-Time LPF Bandwidth Trim	3.0 KHz
Output Buffer Gain Select	2
IAMP Feedback Capacitor Selection	1.007 pF
IAMP Balance Capacitor Trim	8.854 pF
IAMP Balance Trim Capacitor Selection	0.000 pF

THIS PAGE INTENTIONALLY LEFT BLANK

APPENDIX G. MS3110 SETTINGS FOR 10-MICRON UNDERWATER SENSOR (UNDERWATER APPLICATION)

Current Reference Trim	Nominal
Voltage Reference Trim	Nominal
Oscillator Trim	Nominal
Output Buffer Gain Trim	Nominal
Output Buffer Offset Trim	Nominal
Output Buffer Output Offset Level Control	2.25V
Continuous-Time LPF Bandwidth Trim	3.0 KHz
Output Buffer Gain Select	4
IAMP Feedback Capacitor Selection	2.090 pF
IAMP Balance Capacitor Trim	2.660 pF
IAMP Balance Trim Capacitor Selection	0.000 pF

THIS PAGE INTENTIONALLY LEFT BLANK

APPENDIX H. MS3110 SETTINGS FOR GEN 2 MOD 1 UNDERWATER SENSOR (AIR APPLICATION)

Current Reference Trim	Nominal
Voltage Reference Trim	Nominal
Oscillator Trim	Nominal
Output Buffer Gain Trim	Nominal
Output Buffer Offset Trim	Nominal
Output Buffer Output Offset Level Control	2.25V
Continuous-Time LPF Bandwidth Trim	3.0 KHz
Output Buffer Gain Select	2
IAMP Feedback Capacitor Selection	2.660 pF
IAMP Balance Capacitor Trim	8.246 pF
IAMP Balance Trim Capacitor Selection	1.197 pF

THIS PAGE INTENTIONALLY LEFT BLANK

APPENDIX I. MS3110 SETTINGS FOR GEN 2 MOD 2 UNDERWATER SENSOR (AIR APPLICATION)

Current Reference Trim	Nominal
Voltage Reference Trim	Nominal
Oscillator Trim	Nominal
Output Buffer Gain Trim	Nominal
Output Buffer Offset Trim	Nominal
Output Buffer Output Offset Level Control	2.25V
Continuous-Time LPF Bandwidth Trim	3.0 KHz
Output Buffer Gain Select	2
IAMP Feedback Capacitor Selection	1.140 pF
IAMP Balance Capacitor Trim	8.246 pF
IAMP Balance Trim Capacitor Selection	0.000 pF

THIS PAGE INTENTIONALLY LEFT BLANK

APPENDIX J. MS3110 SETTINGS FOR GEN 2 MOD 2 UNDERWATER SENSOR (UNDERWATER APPLICATION)

Current Reference Trim	Nominal
Voltage Reference Trim	Nominal
Oscillator Trim	Nominal
Output Buffer Gain Trim	Nominal
Output Buffer Offset Trim	Nominal
Output Buffer Output Offset Level Control	2.25V
Continuous-Time LPF Bandwidth Trim	3.0 KHz
Output Buffer Gain Select	2
IAMP Feedback Capacitor Selection	2.090 pF
IAMP Balance Capacitor Trim	8.246 pF
IAMP Balance Trim Capacitor Selection	0.000 pF

THIS PAGE INTENTIONALLY LEFT BLANK

APPENDIX K. LOCK-IN AND PREAMP SETTINGS (UNDERWATER TESTING SETUP)

A. 10-MICRON SENSOR SETUP

(1) SR865 Lock-in Amplifier Settings [16]

Sensitivity: 10 mV

Time Constant: 300 msec

Range: 300mV

Filter: 6dB slope

Sweep time: 100 sec

(2) Stanford Research Model SR560 Low Noise PreAmplifier output to Lock-in for Bruel &Kjaer Type 8103 Hydrophone

High-Pass: 30 Hz

Low Pass: 10 kHz

Gain: 2×10^3

B. GEN 2 MOD 2 SENSOR SETUP

(1) SR865 Lock-in Amplifier Settings [16]

Sensitivity: 10 mV

Time Constant: 100 msec

Range: 300mV

Filter: 6dB slope

Sweep time: 100 sec

THIS PAGE INTENTIONALLY LEFT BLANK

LIST OF REFERENCES

[1] R. Miles, D. Robert, and R. Hoy, “Mechanically coupled ears for directional hearing in the parasitoid fly Ormia ochracea,” *J. Acoust. Soc. Am.*, vol. 98, no. 6, pp. 3059–3070, Dec. 1995.

[2] Wilmott, D. *et al.* “Bio-inspired miniature direction finding acoustic sensor,” *Sci Rep.* 6, 29957, 2016, doi:10.1038/srep29957

[3] Touse, M. *et al.* “Fabrication of a micromechanical directional sound sensor with electronic readout using comb fingers,” *Appl. Physics Lett.*, vol. 96, no. 17, 2010.

[4] D. Wilmott, “Direction finding using multiple MEMS acoustic sensors,” M.S. thesis, Dep. Physics, Naval Postgraduate School, Monterey, CA, 2015.

[5] W. Swan, “Bio-inspired MEMS direction finding acoustic sensor for air and underwater applications,” M.S. thesis, Dept. Physics, Naval Postgraduate School, Monterey, CA, 2016.

[6] M.A. Hopcroft, W.D. Nix and T.W. Kenny, “What is Youngs’s modulus of Silicon?” *Journal of Microelectromechanical Systems*, vol. 71, no. 10, Oct. 2000.

[7] *MS3110 Quick Start Setup*, Irvine Sensors Corporation, Costa Mesa, CA, 2004.

[8] Product Data – ½” Free Field Field Microphone – Type 40AF SN 31881 G.R.A.S Sound & Vibration Aps. Calibration Data Sheet.

[9] Polytech Incorporated. (2017, Jul. 24). 500 Micro System Analyzer. [Online]. Available: http://www.polytec.com/us/products/vibration-sensors/microscope-based-systems/msa-500-micro-system-analyzer

[10] T. Klose *et al.*, “Fluidmechanical damping analysis of resonant micromirrors with out-of-plane comb drive,” *Proceedings of the COMSOL Conference*. Hanover, 2008.

[11] L. Kinsler *et al. Fundamentals of Acoustics*, 4th ed. Hoboken, NJ: John Wiley & Sons, Inc., 2012.

[12] R.M. Drake and S.E. Forsythe, “Low frequency hydrophone calibration in a standing/traveling wave tube,” *UAM 2007 Conference* NUWCDIVNPT/USRD 2007

[13] Product Data –Bruel Kjaer– Type 8103 Hydrophone S/N 2241680. Calibration Data Sheet.

[14] R. Downey, “Toward a micro-scale acoustic direction finding sensor with integrated electronic readout,” Ph.D. dissertation, Dept. Physics, Naval Postgraduate School, Monterey, CA, 2013.

[15] Ensinger-Hyde. (2003, Mar.). Delrin data sheet. [Online]. Available: http://www.sdplastics.com/delrin/delrin[1].pdf

[16] *SR865 2MHz DSP Lock-in Amplifier Operation Manual*, Rev 1.29, Stanford Research Systems, Sunnyvale, CA, 2015.

INITIAL DISTRIBUTION LIST

1. Defense Technical Information Center
   Ft. Belvoir, Virginia

2. Dudley Knox Library
   Naval Postgraduate School
   Monterey, California